

Nathan D. Masters,<sup>1,2</sup> Maarten P. de Boer,<sup>1</sup> Brian D. Jensen,<sup>1,3</sup> Michael S. Baker,<sup>1</sup> and David Koester<sup>4</sup>

## Side-by-Side Comparison of Passive MEMS Strain Test Structures under Residual Compression

---

**REFERENCE:** Masters, N. D., de Boer, M. P., Jensen, B. D., Baker, M. S., and Koester, D., "Side-by-Side Comparison of Passive MEMS Residual Strain Test Structures under Residual Compression," *Mechanical Properties of Structural Films, STP 1413*, S. B. Brown and C. L. Muhlstein, Eds., American Society for Testing and Materials, West Conshohocken, PA, Online, Available: [www.astm.org/STP/1413/1413\\_23](http://www.astm.org/STP/1413/1413_23), 15 September 2001.

**ABSTRACT:** Knowledge and control of residual strain is critical for device design in MEMS, and therefore it is important to establish standards for residual strain measurement. In this study, pointer, microring, bent-beam, and fixed-fixed beam test structures are used to evaluate residual strain both theoretically and experimentally. An equation that enables easier evaluation of bent-beam structures is derived. Also, a finite difference model that incorporates the non-idealities of fixed-fixed beams and determines an optimum fit to the measured deflection curve is presented. The model allows accurate residual strain evaluation of each buckled fixed-fixed beam. Experimentally, pointer structures were found to be susceptible to adhesion. Microrings, intended for residual tension assessment, also could not be evaluated because the residual strain was compressive. Bent-beam and fixed-fixed beams could both be evaluated. The main criterion for test structure effectiveness was taken to be the repeatability of residual strain on structures in close proximity; each should exhibit the same value. Using optical microscopy, the residual strain of bent-beams was determined with  $\pm 13 \mu\epsilon$  repeatability based on standard deviation of adjacent structures of similar design. Using optical interferometry, the residual strain of fixed-fixed beams was determined with  $\pm 2 \mu\epsilon$  repeatability based on standard deviation for adjacent beams of different lengths. The strain values obtained from the two structures are in reasonably good agreement. Cantilevers were also evaluated to obtain film curvature values.

**KEYWORDS:** residual strain, MEMS test structures, bent-beams, microrings, pointers, fixed-fixed beams, cantilevers, optical metrology

### Introduction

Polycrystalline silicon (polysilicon), used in integrated circuits and Microelectromechanical Systems (MEMS), is commonly deposited by chemical vapor deposition. Residual strain in polysilicon thin films is a result of the interactions of many factors that may be present during deposition, including thermal environments, dopants, impurities, and grain coalescence, orientation and growth, and surface as well as interfacial stress [1-6]. Because of the importance of residual strain in mechanical design and as a measure of fabrication control, many techniques and structures have been

---

<sup>1</sup> Sandia National Laboratories, PO Box 5800, Albuquerque, NM 87185,  
[www.mdl.sandia.gov/Micromachine](http://www.mdl.sandia.gov/Micromachine)

<sup>2</sup> current address – Mechanical Eng. Dept., Brigham Young University, Provo, UT 84602.

<sup>3</sup> current address – Mech. Eng. Dept., University of Michigan, Ann Arbor, MI 48109-2125.

<sup>4</sup> Cronos Integrated Microsystems, 3026 Cornwallis Rd., Research Triangle Park, NC 27709.

suggested for residual strain measurements. However, it remains difficult to quantify strain to a known accuracy. Further, it is not known whether various laboratories will measure the same value even on the same structures. Usually, low residual strain is desired for device designs, leading to test structure designs that must be highly compliant to enable strain evaluation. Depending on the test structure design, this can lead to adhesion (i.e., stiction) or out-of-plane buckling that can render the test structures ineffective.

To address these issues, a round robin evaluation of test structures was organized and sponsored by the American Society of Testing and Materials (ASTM) Task Group E08.05.03. The intent of the study was to use passive structures that have been previously proposed and that could be easily analyzed. Pointers [7], bent-beams [8,9] microrings [10], and fixed-fixed beams [11-14] were chosen. Cantilevers [15,16] were also studied to obtain stress gradient information. In this paper, we report on the analysis of the test structures made by our group at Sandia National Laboratories. One other group has analyzed its results [17].

To decide how to measure and analyze the test structures, we made the following two considerations. First, nondestructive testing is important for round robin testing, and is also important in general to MEMS. Second, because residual strain can vary across a wafer, from wafer to wafer, and from lot to lot, it is important to quickly yet accurately assess residual strain values. Our analysis criteria are as follows:

- 1) The metrology is only by optical methods.
- 2) Only two-dimensional deflections and analyses are considered.

The first criterion allows for rapid and noncontacting measurements. While scanning electron microscopy (SEM) metrology enables higher resolution for in-plane measurements, we ruled it out as being too expensive and time consuming for routine metrology. Also, any concern that electrostatic charging may induce test structure deflection during the measurement is alleviated. Furthermore, for out-of-plane measurements, optical interferometry is more sensitive than SEM and is well calibrated. The second criterion is in keeping with most of the literature, and reflects our interest in keeping the analysis as simple as reasonably possible.

Given these criteria, our assessment of the test structures is based on addressing the following questions in the Discussion section:

- 1) How well are the critical deflections measured?
- 2) To what degree do the test structure deflections reflect the 2-D analysis?
- 3) How repeatable are the measurements on similar structures in close proximity?
- 4) What are the area requirements?
- 5) How long does it take to determine the strain value?

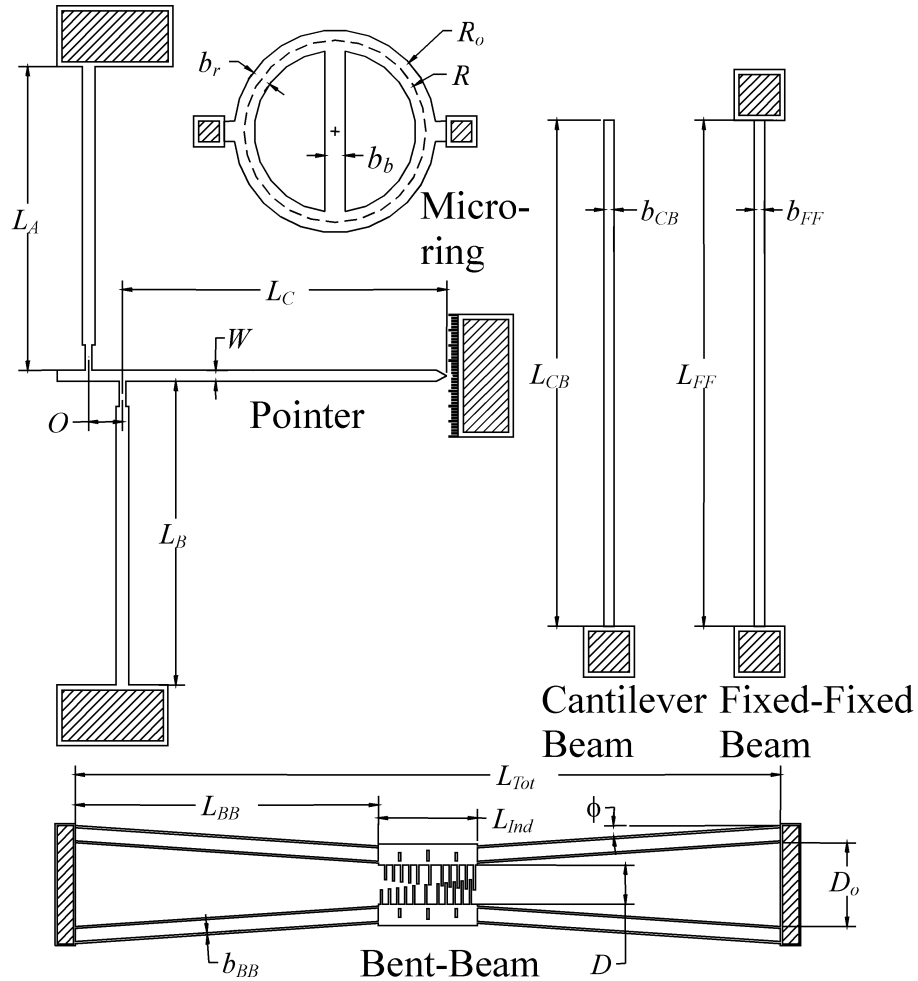


FIG. 1—Test structures used for residual strain evaluation (top views).

### Test Structures and Analysis

The test structures we studied are shown schematically in Fig. 1. Critical geometric parameters for each device are indicated. We present the results of the two-dimensional mechanics analyses in this section. The equations are derived in Appendices A-D. For the pointers (Appendix A) and the microrings (Appendix C), literature references have been used. For the bent-beams (Appendix B), we introduce a new derivation that is simpler to use than previous literature references and applies for the strain range examined here. For idealized fixed-fixed beams (Appendix D), Euler buckling theory is used for first order modeling. This is appropriate because the test structures were under residual compression. Our approach for 2-D finite difference modeling incorporating the effects of boundary compliance in fixed-fixed beam structures is also outlined in this section. Cantilevers, also shown in Fig. 1, are used to measure curvature (allowing the stress gradient to be deduced), and are described in this section along with the fixed-fixed beams.

The analysis for several of the test structures (pointers, microrings, and rigidly supported fixed-fixed beams) can be carried out without knowledge of Young's modulus,  $E$ . However, the analyses for bent-beam sensors and the 2-D finite difference model for

the buckled fixed-fixed beams require  $E$  to be known. We will report the uniaxial residual strain  $\varepsilon_R$  of these devices assuming  $E = 165$  GPa [18]. Uniaxial residual stress  $\sigma_R$  can be calculated from  $\sigma_R = E\varepsilon_R$  (the loading condition of fixed-fixed beams is within 1% of plane stress conditions [19] - therefore no adjustment to  $E$  is made).

In Table 1, we compare the various structures from the point of view of test structure principle, area consumed, typical resolution and strain range, assumed limitations, layout dimensions and comments on the analyses. The test structures can be separated into two main families according to the primary measurement technique used to extract the residual strain value: in-plane (pointers and bent-beams) and out-of-plane (microrings and fixed-fixed beams). The area information in Table 1 is for all the structures on a given level of polysilicon, and the number of associated residual strain measurements is given as well. In making strain resolution comparisons, we assume a  $0.5 \mu\text{m}$  ( $\pm 0.25 \mu\text{m}$ ) deflection resolution for in-plane devices, and a  $10 \text{ nm}$  ( $\pm 5 \text{ nm}$ ) resolution for the out-of-plane measurements. These values stem from the limitations of the brightfield and interferometry optical techniques, respectively. The resolution values reflect the uncertainty in strain measurements due to metrology only. Because these structures are fabricated side-by-side, we obtain information on the relative accuracy of structures in a given family. For absolute accuracy, sensitivity to film thickness, line width, boundary conditions, and 3-D deflections would also have to be considered. Each test structure in Table 1 is discussed next.

### Pointers

Pointers are in-plane test structures that make use of geometric layout to amplify small displacements induced by residual strain (compressive or tensile). The amplified output of the pointer indicator,  $y$ , is measured on a scale attached to the substrate [7]. The support beam lengths,  $L_A$  and  $L_B$ , are typically identical. Increasing the length of  $L_C$  or decreasing the separation distance  $O$  will enhance the amplification effect. Displacement readings at the pointer end are used to calculate the residual strain levels. The analysis in Ref 7, which is repeated in Appendix A, assumes an ideal geometric relationship between residual strain and the displacement of the indicator, augmented by a correction factor,  $C_F$ , derived from finite element models of the devices, resulting in Eq 1,

$$\varepsilon_R = \frac{Oy}{(L_A + L_B)(L_C + O/2)} \frac{1}{C_F}. \quad (1)$$

The area of pointers is relatively large at  $\sim 1 \text{ mm}^2$  per test structure. The resolution is  $40 \mu\text{E}$ , assuming an optical resolution of light microscopy of  $0.5 \mu\text{m}$  ( $\pm 0.25 \mu\text{m}$ ), and dimensions of a studied device ( $L_A = L_B = 490 \mu\text{m}$ ,  $L_C = 575 \mu\text{m}$ ,  $W = 20 \mu\text{m}$ ,  $O = 20 \mu\text{m}$  and  $C_F = 0.425$ ). Three pointers were used here with  $O$  ranging from  $20 \mu\text{m}$  to  $60 \mu\text{m}$ . We determined the values of  $C_F$  for the geometries used here from finite-element analysis over a range of  $\pm 3000 \mu\text{E}$ . Pointers are capable of measuring compressive and tensile residual strain for negative (left) and positive (right) indicator values, respectively. In keeping with the 2-D analysis, the possibilities of buckling across the  $L_A + L_B$  support arms, adhesion to the substrate and strain gradient along the pointer length (which may cause the tip to contact the substrate) are not considered.

TABLE 1—Theoretical and practical residual strain test structure comparisons.

	Pointers	Bent-beams	Microrings	F-F Beams
Principal of Structure	Geometric amplification	Geometric amplification	Conversion of tension to buckling	Buckling deflections converted into strain value
Area <sup>5</sup> (# of devices, # of measurements per poly level)	3.2 mm <sup>2</sup> (3,3)	1.35 mm <sup>2</sup> (6,6)	2.9 mm <sup>2</sup> (14,1)	1.0 mm <sup>2</sup> (5,5)
Resolution (μϵ)	40 ( <i>O</i> = 20 μm)  99 ( <i>O</i> = 60 μm)	12.5 ( <i>L</i> <sub>BB</sub> = 300 μm, ϕ = 33.3 mrad)  5 ( <i>L</i> <sub>BB</sub> = 500 μm, ϕ = 20 mrad)	50	0.7 ( <i>L</i> <sub>FF</sub> = 596 μm, <i>A</i> = 2 μm)
Range (μϵ) (see text)	±3000	-312 to +235 ( <i>L</i> <sub>BB</sub> = 300 μm) -112 to +84 ( <i>L</i> <sub>BB</sub> = 500 μm)	+250 to +900	-15 to -6765
Assumed Limitations	±0.25 μm optical resolution 2-D modeling	±0.25 μm optical resolution 2-D modeling	Discrete measurement 2-D modeling	±5 nm interferometric resolution 2-D modeling
Layout Dimensions of Test Structures in the Class (see Fig. 1)	<i>L</i> <sub>A</sub> = <i>L</i> <sub>B</sub> = 490 μm <i>W</i> = 20 μm <i>O</i> = 20 μm ( <i>C</i> <sub>F</sub> = 0.425), <i>O</i> = 40 μm ( <i>C</i> <sub>F</sub> = 0.530), <i>O</i> = 60 μm ( <i>C</i> <sub>F</sub> = 0.539), (with <i>L</i> <sub>C</sub> = 585, 575, and 565 μm, respectively)	<i>b</i> <sub>bb</sub> = 2 μm <i>D</i> = 38.5 μm <i>L</i> <sub>Ind</sub> = 98 μm ϕ = 33.3, 66.7 and 135.4 mrad ( <i>L</i> <sub>BB</sub> = 300 μm) ϕ = 20.0, 20.0** and 79.5 mrad ( <i>L</i> <sub>BB</sub> = 500 μm)	<i>b</i> <sub>r</sub> = 25 μm <i>b</i> <sub>b</sub> = 10 μm <i>R</i> <sub>0</sub> varies from 97 to 900 μm	<i>L</i> <sub>FF</sub> = 196 μm, 396 μm, 596 μm, 796 μm, and 996 μm <i>b</i> = 18 μm
Comments on Test Structure Modeling	Treats the device as a rigid body mechanism (ignoring elastic deformation). A correction is then made for bending. Out-of-plane deflections and boundary compliance are ignored. Applies to tension and compression.	Ignores out-of-plane deflections and boundary compliance. Applies to tension and compression.	Boundary compliance modeled but not measured. Tensile measurements only.	Reflects the 2-D flexures. Includes boundary compliance and strain gradients. Tensile residual strain can be measured using active techniques.

<sup>5</sup> Area measurements based on representative arrangement of devices on a given structural level: Pointers: Three pointers; Bent-beams: Six bent-beams (\*\*for *L*<sub>BB</sub> = 500 μm, two bent-beams have ϕ = 20 mrad); Microrings: array of 14 rings with radii from 97 to 900 μm; Fixed-fixed beams: array of five fixed-fixed beams (connected to 100 × 100 μm<sup>2</sup> actuation pads).

### Bent-Beams

Bent-beams also take advantage of geometric layout to amplify in-plane displacements induced by residual strain [8,9]. We develop in Appendix B a linear solution. The displacement,  $\delta$ , of the indicators on freestanding structures is measured and the residual strain level is then computed from

$$\varepsilon_R = \delta \frac{\left[ \frac{wt L_{BB}^3 \sin \phi}{\cos^4 \phi} + \frac{12I_{yy} L_{BB}}{\sin \phi} + \frac{6I_{yy} L_{Ind}}{\sin \phi \cos \phi} \right]}{\left[ (2L_{BB} + L_{Ind}) \left( \frac{wt L_{BB}^3}{\cos^3 \phi} - \frac{12I_{yy} L_{BB}}{\cos \phi} \right) \right]}, \quad (2)$$

where  $L$  is the support beam span and  $L_{Ind}$  is the length of the indicator. For the double beam geometry in this study,  $wt = 2(b_{BB}t)$  is the support cross sectional area and  $I_{yy} = 2(tb_{BB}^3/12)$  is the in-plane moment of inertia. Also,  $\phi$  is the support beam angle defined as  $\phi = \arctan[(D_0 - D)/2L_{BB}]$ , as indicated in Fig. 1. Our derivation for Eq 2 is distinct from those in Refs 8 and 9. It considers the residual strain in both the indicators and the supporting beams using Castigliano's theorem<sup>6</sup>. Equation 2 is accurate at low  $|\varepsilon_R|$  values and is independent of  $E$ . Importantly, it is more quickly applied than the approaches in Refs 8 and 9. Also, the effect of  $L_{Ind}$ , not considered in Refs 8 and 9, is accounted for here. However, nonlinear effects, important at high  $|\varepsilon_R|$  values as detailed in Ref 8, are not considered. In Fig. 2, we quantitatively compare the three cases for a specific geometry.

The area of bent-beams is small at  $\sim 0.23 \text{ mm}^2$  per structure. The resolution is  $12.5 \text{ } \mu\text{e}$  assuming an optical resolution of light microscopy of  $0.5 \text{ } \mu\text{m}$  ( $\pm 0.25 \text{ } \mu\text{m}$ ), and a layout representative of the studied devices ( $L_{BB} = 300 \text{ } \mu\text{m}$ ,  $\phi = 33.3 \text{ mrad}$ ,  $b_{bb} = t = 2 \text{ } \mu\text{m}$  and  $L_{Ind} = 98 \text{ } \mu\text{m}$ ). The strain range is defined as shown in Fig. 2. At high residual strain values ( $\varepsilon_R < -313 \text{ } \mu\text{e}$ ,  $\varepsilon_R > 235 \text{ } \mu\text{e}$ , based on 10% deviation in deflection from Ref 8), Eq 2 loses accuracy. However, this is beyond the acceptable strain level of many MEMS processes. It should be noted that for the layout dimensions considered in Fig. 2, the deflection range of the device is  $\pm 10 \text{ } \mu\text{m}$ . If Eq 2 were used over this range, the accuracy would remain within 30%. Bent-beam incremental sensitivity over the entire range of the structure has been discussed in detail [8]. Five geometrical variations were used here, with  $\phi = 33.3, 66.7$  and  $135.4 \text{ mrad}$  ( $L_{BB} = 300 \text{ } \mu\text{m}$ ), and  $\phi = 20.0, 20.0$  and  $79.5 \text{ mrad}$  ( $L_{BB} = 500 \text{ } \mu\text{m}$ ). We note that two structures with  $\phi = 20.0 \text{ mrad}$  at  $L_{BB} = 500 \text{ } \mu\text{m}$  were laid out.

---

<sup>6</sup> Castigliano's theorem is an energy method for determining the elastic deflection of a system. It requires that deflections be linear and elastic. As such the strain energy,  $U$ , stored in the system may be computed as the area under the load-deflection curve (which will be a triangle). The deflection of the system can then be found by differentiating the strain energy with respect to a load,  $P$ , acting in line with the deflection direction of interest  $\Delta = \partial U / \partial P$  (in many cases this is accomplished by virtual loads). This method works for axial, bending, transverse shear, and torsional loading. See for example Ref 20.

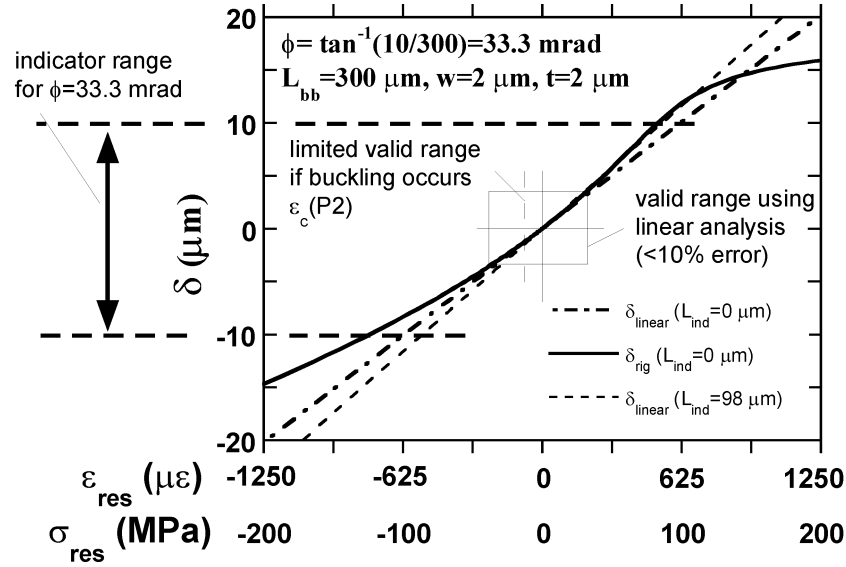


FIG. 2—Comparison between rigorous analysis by Gianchandani ( $\delta_{rig}$ ) to linearized analysis from Appendix B ( $\delta_{linear}$ ) with  $L_{ind}=0$  and  $L_{ind} = 98 \mu m$ .

Bent-beams are capable of measuring compressive and tensile residual strain, indicating compression by a decrease in the distance between the indicators and tension by an increase. Resolution depends on layout geometry. If resolution at low stress values is desired, then  $L_{BB}$  must be large. However, this increases the proclivity of the structure to buckle out-of-plane. For example, if the thickness of the layer is less than the width  $b_{BB}$ , the effective strain range is reduced to  $-45 \mu\epsilon$ , as indicated in Fig. 2 for the Poly2 layer, for which  $t = 1.46 \mu m$  (see experimental section). Figure 2 is discussed in more detail in Appendix B.

### Microrings

Microrings are passive devices proposed by Guckel to measure tensile residual strain [10]. As shown in Fig. 1, a circular ring anchored at two diametrically opposite positions converts tensile residual strain into compressive strain in a crossbeam that is orthogonal to the ring anchors. Ranges (rather than precise measurements) of residual strain levels are determined by observing the transition from unbuckled to buckled crossbeams. The residual strain for the structures is

$$\epsilon_R = \frac{\epsilon_{cr}}{g(R)}, \quad (3)$$

where  $\epsilon_{cr}$  is the critical strain needed to buckle the crossbeam and  $g(R)$  is the conversion efficiency of tensile strain in the ring into compressive strain in the crossbeam. As briefly reviewed in Appendix C, Guckel et al.'s analytical model of the microring derives the effect of the ring to beam width ratio,  $b_r/b_b$ , and  $R$  on  $g(R)$  using Castigliano's method [10]. Also, the effect of boundary rotation on  $\epsilon_{cr}$  is determined. For thin films, the

normal mode of buckling is out-of-plane. If brightfield microscopy is used, detection of buckling requires focal plane adjustments. Interferometry is a more sensitive technique for detecting buckling. As suggested in Ref [7], a critically-buckled test structure is established when the crossbeam center deflection is  $\sim 0.6t$ , where  $t$  is the film thickness.

The area occupied to obtain a single measurement from microrings is large— $2.9 \text{ mm}^2$ . To determine the strain resolution and the range over which residual strain can be measured, Drieënhuizen et al. [7] showed that the number of buckling structures required is

$$N_{\min} = \frac{\log(\varepsilon_{\max} / \varepsilon_{\min})}{\log(1+r)} - 1, \quad (4)$$

where  $N_{\min}$  is the minimum number of structures,  $\varepsilon_{\max}$  and  $\varepsilon_{\min}$  are the upper and lower limit of the desired range of study, and  $r$  is the resolution (in percent) of the measurement. Using this equation we can determine that 40 microrings would be required for a range of 10-500  $\mu\varepsilon$  with a resolution of 10% of the range. In this study, 14 microrings of various sizes were distributed in each level of polysilicon, with a designed resolution of approximately 50  $\mu\varepsilon$  over a range from 250 to 900  $\mu\varepsilon$  tensile.

The microring is in reality a three-dimensional structure. It was demonstrated by 3-D finite element analysis that for small values of  $b_r$ , post-release microring shortening in the beam direction versus the constraining direction increases the critical strain for buckling [21]. Also, increasing the length of the connection supporting the ring decreases the critical strain [21]. Further, the strain gradient has been identified as affecting the flexures of the microring [22], meaning that the entire shape and not only the crossbeam flexures must be measured in order to correctly interpret the structure. We note that interferometric measurements integrated with 3-D modeling could be applied to reduce the required number of microrings. The technique would be similar to but more complicated than that used with cantilever and fixed-fixed beams covered in the next section.

### Fixed-Fixed Beams

Fixed-fixed beams have been used as passive structures for compressive strain measurement by detecting buckling in an array of beams similar to the measurements of microrings [7,10,11,23]. However, the amplitude is sensitive to residual stress in the film, and this allows each buckled beam to be used for residual strain measurement. From Euler buckling theory as in Appendix D, residual strain for each buckled beam is determined from

$$\varepsilon_R = \frac{\pi^2}{L_{FF}^2} \left( \frac{A^2}{4} + \frac{t^2}{3} \right), \quad (5)$$

where  $A$  is the amplitude of the buckling deflection,  $L_{FF}$  is the beam length and  $t$  is the beam thickness. The shape will be sinusoidal according to

$$z(x) = \frac{A}{2} \left( 1 + \cos \frac{2\pi x}{L_{FF}} \right), \quad -L_{FF}/2 \leq x \leq L_{FF}/2. \quad (6)$$

The area of fixed-fixed-beams is small at  $\sim 0.20 \text{ mm}^2$  per structure. Considering that  $A$  can be measured very well by interferometry, Eq 5 is very accurate for

$$L_{FF} > \approx 1.1 L_{cr} = 1.1 \pi t / \sqrt{3\varepsilon_R}, \quad (7)$$

where  $L_{cr}$  is the critical buckling length, as discussed in Appendix D. From Eq 6, the approximate strain resolution is

$$\Delta\varepsilon_R = 5.2 \frac{\Delta A \cdot A}{L_{FF}^2}, \quad (8)$$

where  $\Delta A = 10 \text{ nm}$  is the amplitude uncertainty. For example, with  $\Delta A = 10 \text{ nm}$ ,  $L_{FF} = 596 \text{ }\mu\text{m}$ , and  $A = 2 \text{ }\mu\text{m}$ , a value of  $\Delta\varepsilon_R = 0.7 \text{ }\mu\text{e}$  ( $\pm 0.35 \text{ }\mu\text{e}$ ) is calculated. A lower limit to the strain range of  $15 \text{ }\mu\text{e}$  can be estimated from Eq 5 using values of  $t = 2 \text{ }\mu\text{m}$ ,  $A = 0.05 \text{ }\mu\text{m}$  (minimum detected amplitude) and  $L_{FF} = 996 \text{ }\mu\text{m}$ . Likewise, an upper range of  $6765 \text{ }\mu\text{e}$  can be approximated using values of  $t = 2 \text{ }\mu\text{m}$ ,  $A = 10 \text{ }\mu\text{m}$  and  $L_{FF} = 196 \text{ }\mu\text{m}$  (upper limit of small-slopes assumption in Appendix D). Five beams of lengths from  $196 \text{ }\mu\text{m}$  to  $996 \text{ }\mu\text{m}$  in  $200 \text{ }\mu\text{m}$  increments were used in the layout. Fixed-fixed beams may also be tested electrostatically, allowing extension to the case of residual tension [12-14,24].

The modeling in Appendix D does not take into account non-idealities such as boundary compliance, unloaded beam takeoff angle or strain gradient. To more accurately extract the residual strain, we can compare the full deflection curve (rather than just the amplitude) with a two-dimensional finite difference model (FDM). The FDM incorporates these non-idealities. We have applied it to the case of electrostatically actuated cantilevers [16] and fixed-fixed beams [13,14,24], and apply it in this paper to the case of passively buckled beams. Figure 3a schematically represents the FDM. The beam is discretized into elements having the material and cross section properties of the beam. Using the Bernoulli-Euler equation, deflections are calculated by performing the numeric integrals of successive loading, moment, and angular deflection profiles.

As shown in Fig. 1, cantilevers of dimensions similar to the fixed-fixed beams were also placed on the test chip. Unloaded cantilevers contain curvature information, and their deflection curve is closely approximated by

$$z(x) = \theta_o x + \kappa x^2 / 2, \quad (10)$$

where  $x$  is the position along the beam beginning at the support post. Our procedure to accurately determine unloaded beam takeoff angle  $\theta_o$  and film curvature  $\kappa$  (due to strain gradient through the thickness of the film) from interferometric data has been described in Ref 16. Knowing  $\kappa$  from the cantilever beam, the internal moment due to strain gradient  $M_i$  is assigned according to

$$M_i = -E I \kappa. \quad (11)$$

Figure 3b shows the support post model used in the FDM. Loaded beam takeoff angle  $\theta$  is different from  $\theta_o$  in a cantilever due to the moment in the buckled beam at the support post. The contributions to  $\theta$  are from  $\theta_o$ , the moment due to buckling and  $M_i$ .

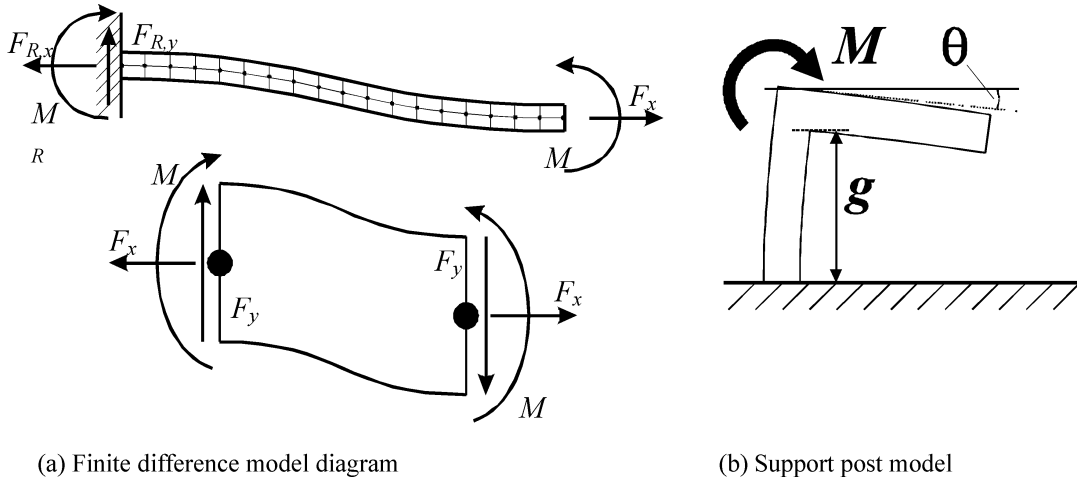


FIG. 3—Finite difference model and support post model diagrams.

The FDM for the case of passively buckled fixed-fixed beams was first compared and shown to agree with Eqs 5 and 6 for rigid boundaries. It also showed excellent agreement with analytical theory that describes the pre- ( $|\epsilon_R| < |\epsilon_{cr}|$ ), transition ( $|\epsilon_R| \sim |\epsilon_{cr}|$ ) and post buckling ( $|\epsilon_R| > |\epsilon_{cr}|$ ) regimes for compliant boundaries [25], as shown in Fig. 4. Finally, as described in Ref 26, negative  $\theta_o$  (cantilever takeoff angle is down) induces downward buckling, while negative strain gradient (cantilever curves down) induces upward buckling. The FDM also agrees with these predictions. These checks validate that the FDM appropriately handles the buckled beam mechanics.

When evaluating deflection curve data in our FDM implementation,  $\theta$  and  $\epsilon_R$  are simultaneously iterated upon in an optimization routine that minimizes the error between the modeled and measured deflection curve. Torsional compliance exerts a measurable effect on the deflection curve. Therefore, unlike Ref 25, this approach does not require finite element analysis of the boundaries conditions as input to the model, because the effect of the boundaries is taken into account by the optimization routine. The analysis here includes only the torsional compliance and not the axial compliance of the boundaries. However, for the beams analyzed in the experimental section, the effect of  $M$  on support post flexures is much larger than that of axial force  $P$ .

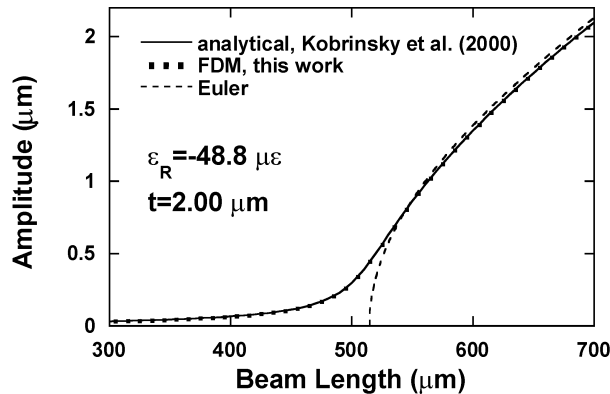


FIG. 4—Using the same boundary conditions, FDM agrees with analytical model for buckling of fixed-fixed beams.

## Experimental

The test structures were processed as part of the Multi-User MEMS Processes (MUMPS™) MUMPS28 fabrication lot. Utilizing conventional surface micromachining technology, MUMPS provides three structural layers of polysilicon. Each of the test structures described above was fabricated side-by-side on a single test chip in the Poly1, Poly2, and Poly1/2 laminate structural layers. The nominal thicknesses of the layers are 2.0, 1.5, and 3.5  $\mu\text{m}$ , respectively, and were measured at  $t = 2.00$ , 1.46, and 3.45  $\mu\text{m}$  using profilometry [27]. The minimum allowable line width for structural layers is 2.0  $\mu\text{m}$ . Typical etch profiles are 88-90°, and typical line width loss from the mask drawing is 0 to 0.2  $\mu\text{m}$ .

The structures were released from the sacrificial oxide layers using an HF acid etch. To minimize stiction, supercritical carbon dioxide drying [28] was applied. After processing, the chips were placed on an adhesive, covered, and sent first to Sandia National Laboratories for analysis. The test structures were fabricated both over a Poly0 ground plane, and over nitride. We report the results of the former only, as they were less susceptible to adhesion (stiction) problems. Our group then sent parts to the next laboratory, which performed its testing, and the round robin continued sequentially. The evaluation period was from February to May, 1999, and a meeting was held in Seattle, Washington in May of 1999 to discuss results of the round robin.

All in-plane deflections were measured using high magnification bright field microscopy (100X objective, NA = 0.9). Magnification will depend on the focus used for each test structure. To minimize variation, the same operator focused and recorded all of the images. Optical micrographs were recorded on a CCD camera. With integrated circuit fabrication techniques, the pitch (linewidth and space) is well known. In-plane calibration was achieved by counting the pixels between Poly0 lines of 20  $\mu\text{m}$  pitch. Transitions in intensity at line edges were used to determine the edge locations. For the 100X objective, a 60  $\mu\text{m}$  length corresponded to 470 pixels, yielding a calibration factor of 0.128  $\mu\text{m}/\text{pixel}$ .

Out-of-plane deflections were measured by interferometry (5X objective, NA = 0.09). As shown in Fig. 5, Michelson interferometry with green light of wavelength  $\lambda = 546$  nm (obtained from an interference filter of 4 nm linewidth (HWF) as characterized by spectrum photometry) was chosen because polysilicon is only weakly transmissive at this wavelength. This eliminates confusion with substrate reflections that arise in multi-wavelength interferometry techniques. Interferometry allows rapid acquisition of qualitative and quantitative out-of-plane deflection data (see Figs. 6–10). Interference patterns result from a difference in phase between the light reflected from the wafer and the reference surface. The resulting image is a superposition of the test structure and the interference pattern with fringes representing contour lines of the out-of-plane deflection. The direction of out-of-plane deflection (up or down) is determined by adjusting the focus and observing the direction of fringe movement. Images were captured on the CCD camera for further analysis. Linescans along the length of the structures are recorded. Each fringe in the interference pattern indicates a deflection of 1/2 wavelength, or 273 nm. Pixel by pixel out-of-plane deflections are extracted by interpolating linescan intensity data. The out-of-plane resolution of this technique is

better than 10 nm/pixel. In-plane pixel length calibration was achieved by measuring a structure of known length, with accuracy of about 1 pixel in 200.

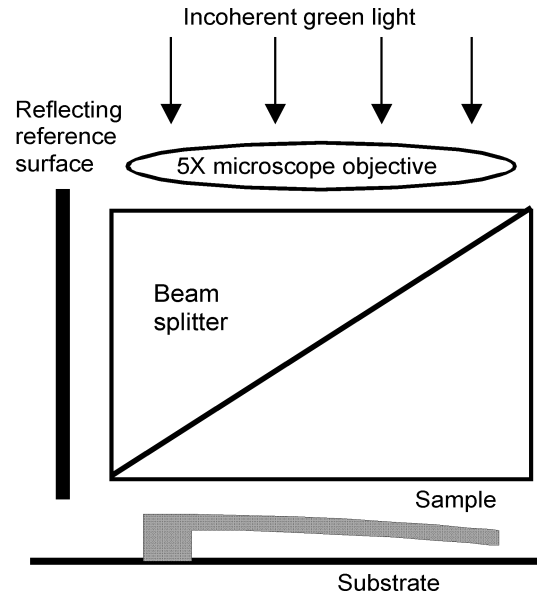


FIG. 5—Schematic of interferometric microscope.

TABLE 2—Qualitative assessment from interferometry.

Test structure	Poly1 Layer	Poly2 Layer	Poly1/2 Layer	Further Study?
Pointers	Adhered (Fig. 6)	Adhered	Adhered	No: adhered
Bent-beams	$L_{BB} = 300 \mu\text{m}$ : free $L_{BB} = 500 \mu\text{m}$ : free minimal out-of-plane deflections	$L_{BB} = 300 \mu\text{m}$ : buckled up ~two fringes $L_{BB} = 500 \mu\text{m}$ : two adhered, one buckled up ~three fringes (Fig. 7)	$L_{BB} = 300 \mu\text{m}$ : free $L_{BB} = 500 \mu\text{m}$ : free minimal out-of-plane deflections	Yes: evaluate effect of buckling for P2 structures
Micro-rings	No flexures apparent: compression (Fig. 8)	Flexures in crossbeams and rings due to stress gradient (Fig. 8)	Not attached to substrate. Not properly anchored	No: incompatible stress state
Canti-levers	$L_{CB} = 196 \mu\text{m}$ : bending down $L_{CB} = 396\text{-}996 \mu\text{m}$ : tip contacting (Fig. 9)	$L_{CB} = 196 \mu\text{m}$ : bending down $L_{CB} = 396 \mu\text{m}$ : tip contacting $L_{CB} = 596\text{-}996 \mu\text{m}$ : long section adhered	$L_{CB} = 196\text{-}596$ and $996 \mu\text{m}$ : bending down $L_{CB} = 796 \mu\text{m}$ : tip contacting (adhesion)	Yes: curvature measurement
Fixed-fixed Beams	$L_{FF} = 196, 396 \mu\text{m}$ : flat $L_{FF} = 596, 996 \mu\text{m}$ : buckled up $L_{FF} = 796 \mu\text{m}$ adhered	$L_{FF} = 196 \mu\text{m}$ : buckled up ~ $\frac{1}{2}$ fringe (Fig. 10) $L_{FF} = 396\text{-}996 \mu\text{m}$ : buckled up many fringes (Fig. 10)	$196\text{-}796 \mu\text{m}$ : flat, $996 \mu\text{m}$ : buckled up ~1 fringe	Yes

For this single image/wavelength technique, quantitative analysis of interferograms (as applied here to the fixed-fixed and cantilever beams) requires that at least one half-fringe be available, that continuous structures be used to avoid phase problems, and that tilt adjustments of the reference surface setting the background fringes parallel to the structures be made. Although the interferometry yields high resolution  $z$ -deflection data,  $x$  and  $z$ -offsets must be determined. The interferometric data near the support post is noisy because of rapid changes in topography. Therefore, linescan data usually begins about 5 to 10 pixels away from the beam. By measuring the first pixel used relative to the support post and knowing the calibration factor, the  $x$ -offset can be adjusted within  $\pm 2$  pixels. Because the interferometric data does not begin at the support post, the  $z$ -offset must also be determined. This is done by comparing the interferometric data to the model data, and assigning an optimum offset for a given model calculation at the first measured pixel.

## Results

### *Qualitative Evaluation*

Qualitative results are summarized in Table 2 and are discussed in this section. Interferometry was first used to evaluate any out-of-plane deflections that might affect the accuracy of the analyses. Pointer structures were plagued by adhesion to the substrate as seen in Fig. 6. The closely spaced fringes near the supports followed by a uniform section with very little contrast indicate that the devices are adhered to the substrate. All pointer structures were affected in a similar manner. A previous study has shown that valid measurements can be obtained from pointer structures adhered in their stress-relaxed position [29]. However, for the low residual strain values observed here, it is difficult to determine the relative contribution to deflections from adhesive forces versus residual strain forces. Therefore, the pointer structures were deemed unusable for further study.

Bent-beam structures fabricated in the Poly2 level are shown in Fig. 7. On the left side of the image where the  $L_{BB} = 300 \mu\text{m}$  long structures reside, a few fringes are visible on the support beams, indicative of small out-of-plane deflections. The deflections are away from the substrate (up). However, on the right side of Fig. 7 where the  $L_{BB} = 500 \mu\text{m}$  long bent-beams are located, more severe out-of-plane distortions are observed on the lower two bent-beams. These deflections are downwards. The structures were adhered to the substrate and therefore these two were not evaluated. The top bent-beam on the right hand side of Fig. 7 is not contacting the substrate, but is buckled up slightly. The bent-beams in the Poly1 and Poly1/2 levels were freely suspended and exhibited small out-of-plane deflections, and they were deemed appropriate for further analysis.

Figure 8 shows microrings in both Poly1 and Poly2. No out-of-plane flexures are observed for the Poly1 microrings, indicating that this layer is either in compression or low tension. Note that both the rings and the crossbeam exhibit roughly equal flexure for the Poly2 level. Both are bending down from a centerline defined by the clamps, which is a manifestation of the strain gradient-induced curvature of the films [22]. This is an excellent example of why it is necessary to consider not only residual strain but also strain gradient when evaluating the microrings. Without the complementary information

from the cantilevers and fixed-fixed beams below, we may have incorrectly inferred that the crossbeams were buckled and that the residual strain in the Poly2 level was tensile. In fact, a tensile state would only be indicated by significantly different out-of-plane flexures for the crossbeam compared to the ring. The Poly1/2 level microrings were not properly anchored to the substrate, and therefore could not be assessed.

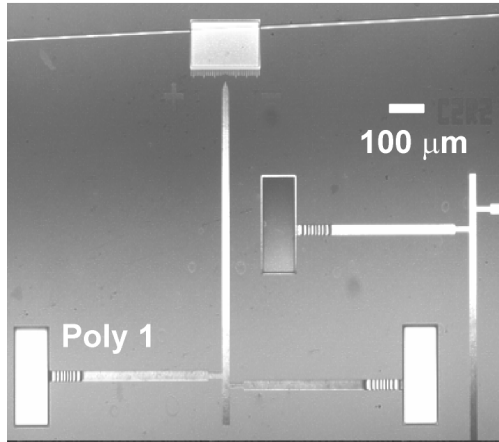


FIG. 6—Interferogram of adhered pointers in Poly1.

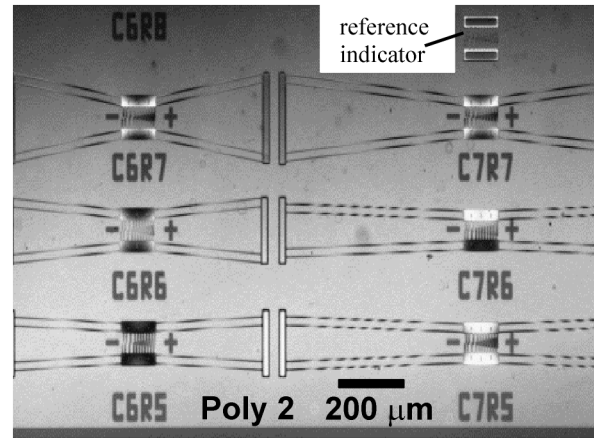


FIG. 7—Interferogram of Poly2 bent beams.  $L_{BB} = 300 \mu\text{m}$  show buckling (left), and  $L_{BB} = 500 \mu\text{m}$  are adhered (lower and middle right).

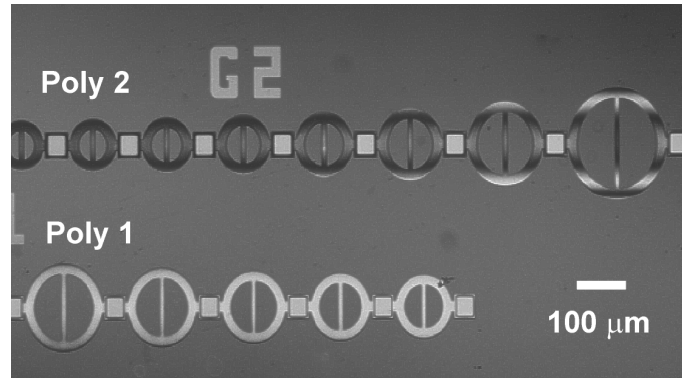


FIG. 8—Interferogram of microrings. Poly2 exhibits a large stress gradient.

An array of Poly1 cantilevers is shown in Fig. 9. From the shortest cantilever (196  $\mu\text{m}$ ), it is clear that the curvature is significant. This cantilever was determined to be bending down. Longer cantilevers were contacting the substrate at their tips because of the large curvature. For the longest cantilever (996  $\mu\text{m}$ ), the substrate imposes an upward force at the tip of the beam that causes its initial deflection beginning at the support post to be upwards. The Poly2 layer exhibited greater out-of-plane deflection than the Poly1 layer, with beams bending down again, and only the shortest cantilever was free. On the other hand, the Poly1/2 laminate exhibited small curvature, and even the 996  $\mu\text{m}$  beam did not contact the substrate. For all layers, free cantilever beams bent down. The cantilever beams were deemed appropriate for obtaining curvature information. However, for the Poly1 and Poly2 layers, data could only be extracted from the shortest cantilever, while for the Poly1/2 layer only the longest cantilever exhibited enough fringe information for quantification.

Short (196 and 396  $\mu\text{m}$ ) Poly1 fixed-fixed beams exhibited no deflection. Longer (596 and 996  $\mu\text{m}$ ) were buckled out-of-plane (upwards). However, the 796  $\mu\text{m}$  Poly1 fixed-fixed beam was adhered to the substrate. A set of Poly2 fixed-fixed beams is shown in Fig. 10, where it can be seen that increasing beam lengths exhibit more fringes. The deflections were upwards, implying the beams were compressively buckled. For the Poly1/2 laminate, all beams were free, but only the longest beam (996  $\mu\text{m}$ ) exhibited a slight upward out-of-plane flexure. Nonadhered, buckled fixed-fixed structures were deemed appropriate for quantitative analysis. From the observed buckling, all layers are in compression.

#### *Quantitative Evaluation*

The qualitative evaluation leads us to eliminate pointers and microrings from further evaluation, leaving one in-plane and one out-of-plane test structure for further study. Summaries of the quantitative analyses are found in Table 3 and in Fig. 11, and are discussed in this section.

*Bent-beams*—The separation between reference indicators fixed to the substrate

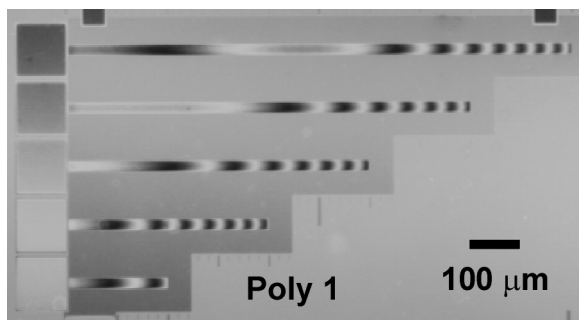


FIG. 9—Interferogram of Poly1 cantilevers. Except for the shortest, all are contacting the substrate at their tips.

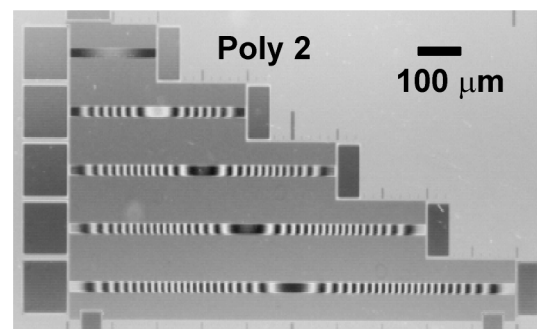


FIG. 10—Interferogram of buckled Poly2 fixed-fixed beams.

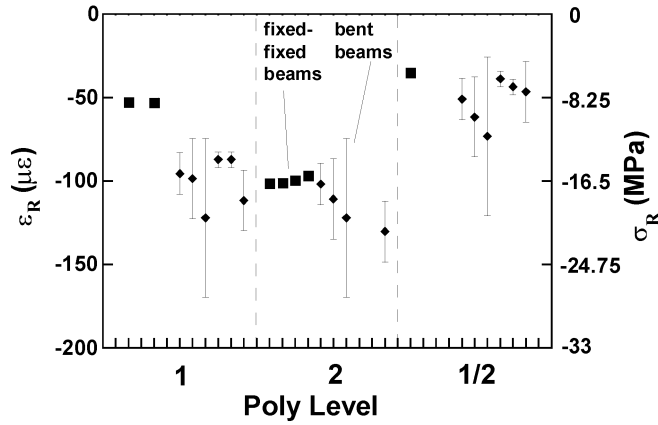


FIG. 11 - Scattergram of fixed-fixed (squares) and bent-beam (diamonds) results.

Fixed-fixed beams: left to right lengths are 996, 796, 596 & 396  $\mu\text{m}$ . Missing data indicates that beams were adhered or not buckled per Table 2 (error bars due to uncertainty in metrology are insignificant).

Bent-beams: left to right  $L_{BB}=300 \mu\text{m}$ , increasing  $\phi$ ,  $L_{BB}=500 \mu\text{m}$  increasing  $\phi$  (error bars due to uncertainty in metrology included). Missing data (Poly2) indicates that bent beams were adhered.

Sample calculation for bent-beams:  
Poly 1 level

$$L_{BB}=300 \mu\text{m}, L_{md}=98 \mu\text{m},$$

$$\phi=33.3 \text{ mrad},$$

$$I_{yy}=2(wt^3/12)=2(2 \cdot 2^3/12)=2.666 \mu\text{m}^4$$

$$wt=2(b_{BB}t)=2(2 \cdot 2)=8 \mu\text{m}^2$$

(2 supports),

$$\delta=(285-300) \text{ pixels} \cdot 0.127 \mu\text{m/pixel}$$

$$=-1.91 \mu\text{m}.$$

Inserting into Eq. (2) yields

$$\epsilon_R = -95 \mu\epsilon$$

For  $\delta=-1.91 \pm 0.25 \mu\text{m}$ ,

$$\epsilon_R = -83, -108 \mu\epsilon$$

(see Fig. 7) was first measured in pixels. Then, the separation between suspended indicators of the bent-beam structure was measured. The difference was multiplied by the calibration factor, and Eq 2 was used to calculate residual strain values. A sample calculation is adjacent to Fig. 11. In Fig. 11, we plot the values of residual strain for each poly level. The error bars indicate error for  $\pm 0.25 \mu\text{m}$  measurement resolution. For larger  $L_{BB}$  and smaller  $\phi$ , the error bars are smaller. The average and standard deviation of residual strain for each poly level is shown in Table 3.

Cantilevers—In Fig. 12, best model fits to the cantilever deflections are shown, along with the deflection data from the interferometry. The Poly1/2 level is the flattest layer, and Poly2 is the layer with the greatest curvature. Agreement between model and data is better than 4 nm/pixel. Results for  $\kappa$  and  $\theta_o$  are tabulated in Table 3. From contour plots in  $(\kappa, \theta_o)$  space that evaluate the difference between the measured and model deflections [16], we can evaluate the confidence regime of the  $\kappa$  and  $\theta_o$  values. To 95% confidence, the values of  $\theta_o$  are accurate within  $\pm 50 \mu\text{rad}$  (implying that  $\theta_o$  is different from 0), while the values of  $\kappa$  are accurate within  $\pm 2 \text{ m}^{-1}$  for Poly1 and Poly2, and within  $\pm 0.2 \text{ m}^{-1}$  for Poly1/2. Note that the magnitude of  $\theta_o$  correlates reasonably well with stress gradient ( $E\kappa$ ), and as we shall see next, with  $\epsilon_R$ . This is in agreement with observations in Ref 15.

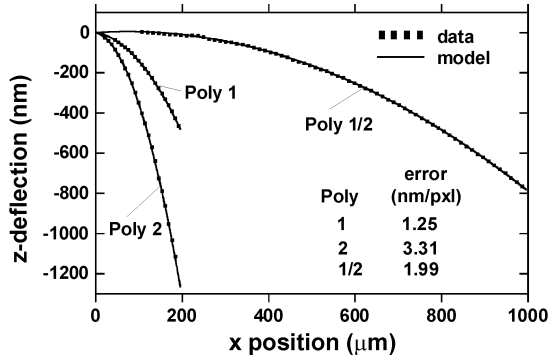


FIG. 12—Measured and modeled deflections of cantilevers.

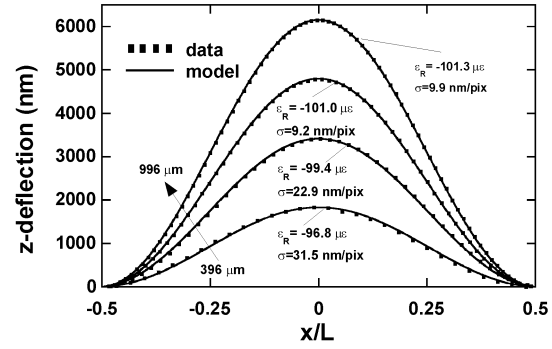


FIG. 13—Poly2 deflections for 396, 596, 796, 996  $\mu\text{m}$  long buckled fixed-fixed beams.  $\sigma$  is the error per pixel.

*Fixed-Fixed Beams*—Using the finite difference model described in Section 2.4, and including the values of strain gradient determined for cantilevers, best fits to the measured deflection curves were found and associated  $\epsilon_R$  values were calculated. Four different beam lengths are shown in Fig. 13 for the Poly2 fixed-fixed beams. The larger errors per pixel between modeled and measured data (10–30 nm/pixel) compared to the cantilevers are mainly due to a small offset in the measured heights of the two ends. This is likely not real, and can be reduced by making a linear correction to the data. Such a correction would affect the values of  $\epsilon_R$  by less than 2%. For Poly1, the critical buckling length is  $L_{cr} = \pi t / \sqrt{3|\epsilon_R|} = 499 \mu\text{m}$  ( $|\epsilon_R| = 52.9 \mu\epsilon$  and  $t = 2.0 \mu\text{m}$ ). Therefore, the 996 and 596  $\mu\text{m}$  Poly1 fixed-fixed beams were also in the post buckled state (the 796  $\mu\text{m}$  Poly1 fixed-fixed beam was adhered to the substate), consistent with  $L_{cr}$ . For Poly2,  $L_{cr} = 265 \mu\text{m}$  ( $|\epsilon_R| = 100 \mu\epsilon$ , with  $t = 1.46 \mu\text{m}$ ). Therefore, the fixed-fixed Poly2 beams of Figs. 10 and 13 are also in the post buckling regime (the 196  $\mu\text{m}$  beam is in a pre-buckled state,  $L_{FF} < L_{cr}$ , and did not present enough fringe information for analysis). The Poly1/2 996  $\mu\text{m}$  fixed-fixed beam was only weakly buckled. With  $|\epsilon_R| = 35.1 \mu\epsilon$  and  $t = 3.45 \mu\text{m}$ ,  $L_{cr}$  is 1056  $\mu\text{m}$ . This confirms that the boundary compliance is responsible for the apparent buckling of the longest Poly1/2 fixed-fixed beam, and that it is in the transition buckling regime.

TABLE 3—Quantitative residual strain results ( $N$ — number of structures evaluated).

Layer	Bent-beams		Fixed-fixed beams		Cantilevers		N
	$\epsilon_R$ (st. dev.) $\mu\epsilon$	N	$\epsilon_R$ (st. dev.) $\mu\epsilon$	N	$\kappa \text{ m}^{-1}$	$\theta_0$ ( $\mu\text{rad}$ )	
Poly1	-100 (13.9)	6	-52.9 (0.2)	2	-21.58	-344	1
Poly2	-118 (12.5)	4	-99.6 (2.1)	4	-60.59	-536	1
Poly1/2	-52 (12.8)	6	-35.1 (N/A)	1	-1.82	+139	1

TABLE 4—*Evaluation of assessment criteria<sup>a</sup> for test structures.*

<sup>a</sup>Assessment criteria for test structures:

- 1) How well are the critical deflections measured?
- 2) To what degree do the test structures reflect the 2-D analysis?
- 3) How repeatable are the measurements on similar structures in close proximity?
- 4) What are the area requirements?
- 5) How long does it take to determine the strain value?

<sup>a</sup> Crit.	<b>Fixed-fixed beams</b>
(1)	Out-of-plane deflection resolution is $\pm 5$ nm. Deflection measurements are made along the entire length of the structures, and the model is optimized to minimize the difference.
(2)	Deflections are essentially two-dimensional. The 2-D FDM captures the physical effects of strain gradient and boundary compliance. Agreement between the model and the data is excellent with typical error differences between the model and the data of 20 nm/pixel.
(3)	Beams in the same structural level but of different lengths yielded the same value of residual strain within 2 $\mu\epsilon$ standard deviation (Table 3).
(4)	The area required is 0.2 mm <sup>2</sup> per measurement (Table 1).
(5)	Taking and analyzing the interferograms requires about 15 minutes per beam. Setting up for the FDM code run requires about ten minutes. The code converges within about one minute.
	<b>Bent-beams</b>
(1)	In-plane resolution is $\pm 0.25$ $\mu\text{m}$ . Only one deflection point on the structure is measured.
(2)	The design of these structures is forced to be more compliant so that strain resolution improves, but this makes them as susceptible to adhesion or to buckling. The flexures are clearly 3-dimensional for the Poly2 layer. However, the implications of this are minor, as addressed in the discussion.
(3)	Beams in the same structural level but of different sizes yielded the same value of residual strain within 14 $\mu\epsilon$ standard deviation (Table 3).
(4)	The area required is 0.23 mm <sup>2</sup> per measurement (Table 1).
(5)	Time to measure is about 15 minutes per structure. Analysis requires only a few minutes using Eq 2.
	<b>Pointers</b>
(1)	In-plane resolution of $\pm 0.25$ $\mu\text{m}$ . Only one deflection point on the structure is measured.
(2)	Flexures did not satisfy the 2-D model due to adhesion to the substrate. Substrate interference can also be caused by buckling or out-of-plane bending from stress gradient.
(3)	Not able to assess repeatability due to substrate adhesion. At 40 $\mu\epsilon$ , the resolution for use in measuring residual strain is low.
(4)	The area requirements are large, 1.0 mm <sup>2</sup> per measurement (Table 1).
(5)	Time to measure is about 15 minutes per structure. Analysis requires only a few minutes using Eq 1.
	<b>Microrings</b>
(1)	Interferometry can be used to sensitively detect buckling. A critical structure must be defined, e.g., by $A = 0.6t$ , because of the gradual transition to cross beam buckling for ring supports.
(2)	Out-of-plane deflections may be due to strain gradient rather than buckling. This can be detected in interferograms, but requires that the user make the distinction between stress gradient and stress, as discussed in Ref 22.
(3)	Cannot report repeatability data for these structures because compression rather than tension observed. Microrings do not have high resolution at 50 $\mu\epsilon$ .
(4)	The area requirements are large, 2.9 mm <sup>2</sup> (Table 1).
(5)	Evaluation time is just a few minutes.

Results for all the fixed-fixed beams are given in Table 3, and graphed against the bent-beams in Fig. 11. The standard deviation of these measurements is less than  $2.1 \mu\text{e}$  or less for adjacent structures in each of the Poly1 and Poly2 layers.

## Discussion

### *Assessment of the Test Structures*

*The assessment criteria, questions (1)-(5) from the Introduction, are considered in Table 4, in order of the experimental effectiveness of the test structures. In addition, we make further comments on each test structure in this section.* **Fixed-Fixed Beams**—The fixed-fixed beams listed at the top of Table 4 yielded the highest resolution and most repeatable results. Further advantages of the fixed-fixed beam structures should be mentioned. First, if the post-buckled state is confirmed, the FDM code is not necessary. For the post-buckled beams, use of Eq 5 rather than the FDM model results in less than a 3% difference in the residual strain results. This indicates that the effect of boundary compliance on the residual strain measurements are small, as expected for post-buckled beams. The further into the post-buckled regime, the less the boundary compliance affects the buckled geometry and therefore the measured residual strain. The FDM is needed principally for evaluation of the transition- and prebuckled beams. Second, comparing the adhesion results, the fixed-fixed beam stiffness is comparable to that of the bent-beam sensors, and greater than the pointer structures. Third, because the structures are wide ( $18 \mu\text{m}$ ), their area moment of inertia is relatively insensitive to process-induced nonidealities such as line width loss and nonvertical sidewalls. Also, because they are much wider than they are tall, there will be no buckling ambiguity (the buckling will be out-of-plane). Fourth, to obtain the intrinsic  $\epsilon_R$  accuracy of fixed-fixed beams, it is essential to apply interferometry. It was originally proposed to use the transition from pre- to post-buckling with SEM or bright field microscopy to determine residual strain [11]. Using this criterion, repeatability of fixed-fixed beams for residual strain measurement was seen to be inferior to pointer structures [7]. More recently however, deflection curve measurements of post-buckled beams has also successfully been used by other authors to accurately determine residual stress [30,31]. For these reasons as well as those listed in Table 4, fixed-fixed beams measured by interferometry yielded the best residual strain measurement in this study.

It is also important to address the limitations of the fixed-fixed beams. First, the model assumed in the FDM for boundary conditions is oversimplified. Real boundaries are more complicated, as shown by finite element method simulations [24]. In particular, they exhibit a nonzero axial deflection,  $\delta_0$ , that can significantly affect results, i.e., by  $(2\delta_0/L_{FF})$ . When possible, it is best to use long beams where boundary conditions are less important. Second, our experience indicates that the method of interferometry we used works best when there are at least several fringes present on the structure of interest. For very small deflections, errors in the deflection measurement become important. For example, the background fringes on the substrate are aligned parallel to the beam of interest. Small rotation error ( $\sim 5^\circ$ ) in the background fringes can become important in inferring small out-of-plane deflections. These corrections are commonly made with commercially available interferometers. Third, the fixed-fixed beams fortuitously

buckled up rather than down, allowing even the longest beams with up to 6 mm amplitude to be analyzed. With a 2  $\mu\text{m}$  support post height, the substrate would have interfered with the buckling had the beam deflections been downward, rendering the long beams unusable for residual strain evaluation. Our analysis indicates that the fixed-fixed beams should have buckled down because of the negative takeoff angles in the cantilevers. We believe that the buckling likely occurred before the release etch was completed. Then, before the oxide clears near the support posts, the downward curvature due to stress gradient would induce the fixed-fixed beams to buckle up. Fourth, cantilever curvature was used to refine the FDM result. The effect on  $\epsilon_R$  was found to be minor ( $< 0.1\%$  change). However, if films were more highly curved downwards, the correction would be more significant. Then, even shorter cantilevers would be necessary to avoid contact with the substrate to enable this correction. Also, for large curvatures, a concave or convex three-dimensional surface can be expected in cantilever and fixed-fixed beams, and therefore the deflections would become three-dimensional.

*Bent-Beams*—The most important conclusion from Table 4 is that based on the standard deviation value, the measurement repeatability of the bent-beams is about five times higher than for the fixed-fixed beams. Comparing the results for Poly2 and Poly1/2, the agreement between the bent-beam and fixed-fixed beam structures is reasonable. However, as seen in Fig. 11 for Poly1, the fixed-fixed beams indicate a smaller magnitude of compression than do the bent-beams. Although we have no satisfactory explanation, several factors can be considered in an attempt to rationalize this disagreement. First, the supports of the bent-beams can buckle out-of-plane, a feature not considered in the 2-D analysis of the bent-beams. This will act to relieve strain, but should decrease rather than increase in-plane deflections, resulting in a lower residual strain reading, which is opposite to the observation. For Poly2, the cross section moment of inertia for out-of-plane bending,  $I_{zz}$  ( $b_{BB}t^3/12$ ), is about one half of the moment of inertia for in-plane bending,  $I_{yy}$  ( $b_{BB}^3t/12$ ), and indeed about two fringes are seen in the interferograms of the  $L_{BB} = 500 \mu\text{m}$  structures, corresponding to an amplitude of 0.5  $\mu\text{m}$ . The strain relieved is negligible as can be calculated from  $\Delta\epsilon = (A\pi/2L)^2 = 0.5 \mu\epsilon$  (from Eq D8, where  $\Delta\epsilon = \epsilon_R - \epsilon_c$ ). This explains how the agreement can be good between the two types of structures for the Poly2 level in spite of the buckling. Meanwhile for Poly1 and Poly1/2, minor out-of-plane buckling is expected and observed because  $I_{zz}$  is equal to or greater than  $I_{yy}$ . Second, the internal moment due to strain gradient is not assessed in the 2-D bent-beam analysis. However, based on the fixed-fixed beam results, this effect is minor. Third, line width may be incorrect by up to 0.2  $\mu\text{m}$  due to overexposure and overetching. Evaluation shows that this will affect the strain readings by only 1  $\mu\epsilon$  or less. Fourth and most likely, some nonsystematic error such as improper focusing on the Poly1 structures may have caused the disagreement.

*Pointer Structures*—These structures are significantly larger than bent-beams because their intrinsic resolution is low. A folded-beam indicator structure with improved geometric amplification over pointer structures has recently been proposed [32] and optimized [33]. This structure requires an area about twice that of the bent-beam sensors, has similar sensitivity, is also evaluated by taking a measurement at a single point, and a simple equation applies. One concern is that the authors rely on sticking of the structures to the substrate, but do not account for the extra strain that is induced when

inferring stress.

*Microrings*—These are intended for measuring tensile residual strains and thus are not suited for the compressive states we found to be present here. Care must be taken not to mistake strain gradient for residual tensile stress.

#### *Strain Properties of the Laminate*

We investigated the idea that the laminate properties might be a simple composite of Poly1 and Poly2. Using residual strain and strain gradient measurements obtained from the cantilever and fixed-fixed beams and assuming a superposition model for noninteracting layers, values of  $\kappa = -28.4 \text{ m}^{-1}$  and  $\epsilon_R = -72.9 \mu\epsilon$  were calculated. The measured values were considerably different:  $\kappa = -1.82 \text{ m}^{-1}$  and  $\epsilon_R = -35.1 \mu\epsilon$  as seen in Figs. 14 *a* and *b*. To investigate this discrepancy, transmission electron microscopy (TEM) was applied to look for microstructural or nucleation differences of Poly2 on oxide versus on Poly1.

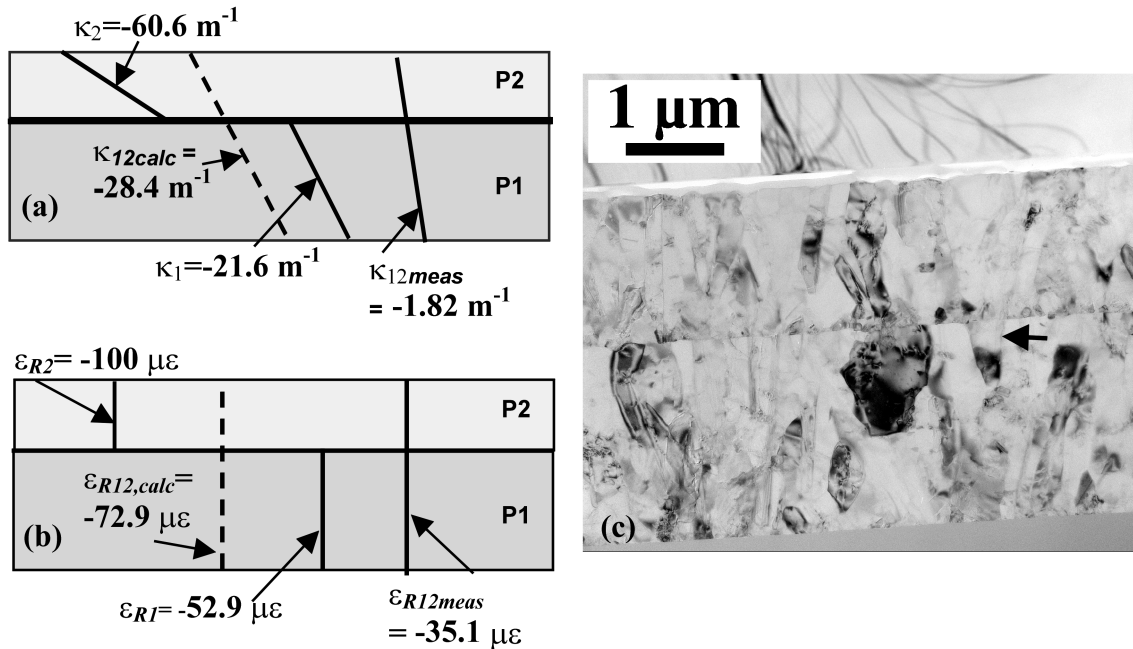


FIG. 14—Using the properties of P1 and P2 individually, the P12 laminate properties for (a) (steeper line implies lesser strain gradient) and (b)  $\epsilon_R$  were predicted and measured (subscripts on  $\epsilon$  and  $\kappa$  denote Poly layers). (c) TEM reveals a small degree of templating, as indicated by the arrow.

A thin oxide at the Poly1/Poly2 interface indicates that the layers should not interact. However, there is a small degree of templating of Poly2 on Poly1, as can be seen in Fig. 14c, and this may be related to the large differences in the predicted versus measured laminate properties. Other features noted in both Poly1 and Poly2 layers include nucleation of grains at the interface, with growth processes resulting in some through-thickness grains of a given poly level. Also, some stacking faults and microtwins are observed, similar to Ref 2.

*Case of Tensile Residual Stress*

We were only able to evaluate the performance of these test structures in compressive residual strain. It is desirable to have structures that measure both tension and compression so that a single set of devices and test procedures are used, and area requirements are minimized. We now consider which devices would have been the best had the residual strain been tensile.

Pointer structures would not suffer as much from adhesion. However, film curvature can still cause interference from the substrate. The theoretical resolution of pointers is low. In tension, microrings would work within the limitations described, i.e., resolution is dependent on the number of rings and space requirements are large. Both pointers and microrings are earlier MEMS developments (early 1990s and late 1980s, respectively) intended mainly to look at higher states of strain than observed in the present study. As MEMS matures, residual strains are decreasing to near zero, and more sensitive test structures and metrologies are required to accurately assess residual strain levels.

Bent-beams exhibit higher resolution than the pointer and microrings, and under tension would also be less likely to suffer from adhesion. Additionally, buckling would not occur, resulting in a situation that more closely matches the model conditions. However, resolution is lower than for the fixed-fixed beams. Use of active methods allows extension of the fixed-fixed beam test structures to the case of residual tension [12–14,24]. Furthermore, active methods allow additional validation of residual stress values of buckled beams. The deflections due to electrical loads at different voltages are compared to models that include the applied electrical load as a function of beam height, and are highly sensitive to residual strain. Once implemented, electrical actuation adds little in cost or time to the measurement process and can be used to obtain and average multiple data points from beams subject to either tensile or compressive residual strain. An integrated platform to accomplish interferometry of actuated devices at the wafer scale is under development [34].

*Recommendations for the Next ASTM Round Robin*

For the next ASTM residual strain round robin, we recommend investigating the bent-beam, folded beam [33], cantilever and fixed-fixed beam test structures in more detail. A significant drawback in the current study is that the number of test structures assessed is small (see Table 3). In the next study, only structures over Poly0 ground pads should be used, and some of the same exact geometries should be laid out side-by-side for improved repeatability quantification. Beams with more length variations should be employed to enable detailed study of the pre- and transition-buckling regimes. We also recommend that participants be equipped with interferometry so that the full deflection curves of beams can be compared. We have observed inconsistent deflection measurements when using a multi-wavelength interferometer (i.e., different results at different magnifications, and different results from profilometry). We believe this is due to the different transmission coefficient of light through silicon at different wavelengths. The effectiveness of a green interference filter in improving the reliability of the measurements on polysilicon structures should be further investigated.

## Summary and Conclusions

The most important result of this study is summarized in Fig. 11, which shows that there is reasonable agreement between the bent-beam sensors and the beam structures. It also shows that especially good repeatability and small uncertainty is possible with post-buckled beam structures measured by optical interferometry. We now state the major conclusions:

- (1) It is important to assess whether fabricated test structures satisfy the 2-D analyses that have been offered. Interferometry is a valuable tool in evaluating the 3-D flexures of the structures. We found that the flexures of fixed-fixed beam and bent-beam structures are essentially 2-D, while microrings can exhibit 3-D flexures because of strain gradient, which can cause the sign of residual strain to be incorrectly inferred. If test structures are adhered to the substrate, it is difficult to determine to what degree their flexures are due to adhesive versus residual strain forces, especially at the low residual strain levels typically achieved in MEMS. Any adhered structures were ruled out from further study because of adhesion to the substrate.
- (2) Because of the high resolution afforded by interferometry, which can be used to obtain nanometer scale measurements across the length of structures, the standard deviation of  $\varepsilon_R$  values measured on geometrically different test structures on the same poly level is about  $2 \mu\varepsilon$  for the fixed-fixed beam structures, The standard deviation was  $13 \mu\varepsilon$  for the bent-beams, likely because of the lower resolution in-plane metrology.
- (3) For the case of post-buckled beams, it was found that the non-idealities affect the residual strain measurement only to second order. A simple measurement of the amplitude of post-buckled beams, coupled with Eq (5), allows  $\varepsilon_R$  to be determined with high repeatability.
- (4) The main importance of the cantilevers is as an aide in understanding the flexures of other structures (e.g., the buckling direction of fixed-fixed beams, the curvature of microrings).
- (5) The strain measurements from the beam structures indicate that the strain state is different for polysilicon when grown on oxide versus polysilicon. The sensitive measurements enabled by the interferometry motivated us to find a microstructural difference in Poly2 on oxide versus on Poly1. With TEM, we were able to resolve some templating of Poly2 on Poly1, which may be responsible for this interactive effect.
- (6) If the state of residual strain is tensile rather than compressive, the fixed-fixed beam test structures also will exhibit significant advantages over the other test structures. In that case, however, active techniques must be employed. Such techniques are under development [34]. Bent-beam structures are a reasonable alternative in the absence of active methods.

*Acknowledgments*

Sandia is a multiprogram laboratory operated by Sandia Corporation, a Lockheed Martin Company, for the United States Department of Energy under Contract DE-AC04-94AL85000. We would like to acknowledge Paul G. Kotula at Sandia National Laboratories for electron microscopy work.

**References**

- [1] Kamins, T. I., "Design Properties of Polycrystalline Silicon," *Sensors and Actuators A*, Vol. 21-23, 1990, p. 817.
- [2] Krulevitch, P., Johnson, G. C., and Howe, R. T., "Stress and Microstructure in Phosphorus Doped Polycrystalline Silicon," *Materials Research Society Proceedings*, Vol. 202, 1992, pp. 79–84.
- [3] Adamaczewska, J. and Budzynsky, T., "Stress in Chemically Vapour-Deposited Silicon Films," *Thin Solid Films*, Vol. 113, No. 4, 1984, p. 271.
- [4] Maier-Schneider, D., Koepurueluelue, A., Ballhausen Holm, S. and Obermeier, E., "Elastic Properties and Microstructure of LPCVD Polysilicon Films," *Journal of Micromechanical Microengineering*, Vol. 6, 1996, p. 436.
- [5] Fuertsch, M., Offenber, M., Muenzel, H. and Morante, J. R., "Influence of Anneals in Oxygen Ambient on Stress of Thick Polysilicon Layers," *Sensors and Actuators A*, Vol. 76, 1999, p. 335.
- [6] Floro, J. A., Hearne, S. J., Hunter, J. A., Kotula, P. G., Chason, E., Seel, S. C., and Thompson, C. V., "The Dynamic Competition Between Stress Generation and Relaxation Mechanisms During Coalescence of Volmer-Weber Thin Films," *Journal of Applied Physics*, Vol. 89, No. 9, 2001, p. 4886.
- [7] van Drieënhuizen, B. P., Goosen, J. F. L., French, P. J., and Wolffenbuttel, R. F., "Comparison of Techniques for Measuring Both Compressive and Tensile Stress in Thin Films," *Sensors and Actuators A*, Vol. 37–38, 1993, p. 756.
- [8] Gianchandani, Y. B. and Najafi, K., "Bent-Beam Strain Sensors," *Journal of Micromechanical Systems*, Vol. 5, No. 1, 1996, p. 42.
- [9] Zavracky, P. M., Adams, G. G., and Aquilino, P. D., "Strain Analysis of Silicon-On-Insulator Films Produced By Zone Melting Recrystallization," *Journal of MEMS*, Vol. 4, No. 1, 1995, p. 42.
- [10] Guckel, H., Burns, D., Rutigliano, C., Lovell, E., and Choi, B., "Diagnostic Microstructures for the Measurement of Intrinsic Strain in Thin Films," *Journal of Micromechanical Microengineering*, Vol. 2, 1992, p. 86.
- [11] Guckel, H., Randzaao, T., and Burns, D. W., "A Simple Technique for the Determination of Mechanical Strain in Thin Films With Applications to Polysilicon," *Journal of Applied Physics*, Vol. 57, No. 5, 1985, p. 1671.
- [12] Osterberg, P. M. and Senturia, S. D., "M-Test: A Test Chip for MEMS Material Property Measurement Using Electrostatically Actuated Test Structures," *Journal of MEMS*, Vol. 6, No. 2, 1997, p. 107.
- [13] Jensen, B. D., de Boer, M. P. and Miller, S. L., "IMaP: Interferometry for Materials Property Evaluation in MEMS," *MSM '99*, San Juan, Puerto Rico, 1999, pp. 206–209.
- [14] Jensen, B. D., de Boer, M. P., and Bitsie, F., "Interferometric Measurement for

- Improved Understanding of Boundary Effects in Micromachined Beams," *Proceedings of the SPIE*, Vol. 3875, Santa Clara, CA, 1999, pp. 61–72.
- [15] Fang, W. and Wickert, J. A., "Determining Mean and Gradient Residual Stresses in Thin Films Using Micromachined Cantilevers," *Journal of Micromechanical Microengineering*, Vol. 6, 1996, p. 301.
- [16] Jensen, B. D., de Boer, M. P., Masters, N. D., Bitsie, F. and LaVan, D. A., "Interferometry of Actuated Cantilevers to Determine Material Properties and Test Structure Non-Idealities In Mems," *Journal of MEMS*, Vol. 10, No. 3, 2001, *in press*.
- [17] Marshall, J. C., "Length and Strain Measurements Using An Optical Interferometer," NIST Internal Report NISTIR 6779, 2001.
- [18] Sharpe, W. N., Yuan, B., and Edwards, R. L., "A New Technique for Measuring the Mechanical Properties of Thin-Films," *Journal of MEMS*, 1997, Vol. 6, No. 3, 1997, p. 193.
- [19] Gupta, R. K., "Electrostatic Pull-In Test Structure Design For In-Situ Mechanical Property Measurement of MEMS," Ph. D. Thesis, Massachusetts Institute of Technology, 1997, 82 pages.
- [20] Juvinall, R. C., *Stress, Strain and Strength*, First ed., New York, McGraw-Hill, 1967.
- [21] Boutry, M., Bosseboeuf, A., Grandchamp, J. P., and Coffignal, G., "Finite-Element Method Analysis of Freestanding Microrings for Thin Film Tensile Strain Measurements," *Journal of Micromechanical Microengineering*, Vol. 7, 1997, p. 280.
- [22] Boutry, M., Bosseboeuf, A., and Coffignal, G., "Characterization of Residual Stress in Metallic Films on Silicon With Micromechanical Devices," *Proceedings of the SPIE*, Vol. 2879, 1996, pp. 126–134.
- [23] Marshall, J. C., Read, D. T., and Gaitan, M., "Analysis of Fixed-Fixed Beam Structures," *Proceedings of the SPIE*, Vol. 2880, 1996, pp. 46–55.
- [24] Baker, M. S., de Boer, M. P., Smith, N. F., and Sinclair, M. B., "Measurement of Residual Stress in MEMS to Sub Megapascal Accuracy," *Journal of MEMS*, submitted.
- [25] Kobrinsky, M. J., Deutsch, E. R., and Senturia, S. D., "Effect of Support Compliance and Residual Stress on the Shape of Doubly Supported Surface Micromachined Beams," *Journal of Micromechanical Systems*, Vol. 9, No. 3, 2000, p. 361.
- [26] Fang, W. L., Lee C. H., and Hu, H. H., "On The Buckling Behavior of Micromachined Beams," *Journal of Micromechanical Microengineering*, Vol. 9, No. 3, 1999, p. 236.
- [27] <http://www.memsrus.com/cronos/svcsdata28.html>, .
- [28] Mulhern, G. T., Soane, D. S., and Howe, R. T., "Supercritical Carbon Dioxide Drying of Microstructures," *Proceedings, 7th International Conference on Solid-State Sensors and Actuators, Transducers '93*, Vol. , Yokohama, Japan, 1993, pp. 296–299.
- [29] Elbrecht, L., Storm, U., Catanescu, R., and Binder, J., "Comparison of Stress Measurement Techniques in Surface Micromachining," *Journal of*

- Micromechanical Microengineering*, Vol. 7, 1997, p.151.
- [30] Chan, E. K., Garikipati, K., and Dutton, R. W., "Comprehensive Static Characterization of Vertical Electrostatically Actuated Polysilicon Beams," *IEEE Design and Test of Computers*, Vol. 16, No. 4, 1999, p. 58.
- [31] Nicu, L., Temple-Boyer, P., Bergaud, C., Scheid, E., and Martinez, A., "Energy Study of Buckled Micromachined Beams for Thin Film Stress Measurements Applied to SiO<sub>2</sub>," *Journal of Micromechanical Microengineering*, Vol. 9, 1999, p. 414.
- [32] Lin, L., Pisano, A. P., and Howe, R. T., "A Micro Strain Gauge with Mechanical Amplifier," *Journal of MEMS*, Vol. 6, No. 4, 1997, p. 313.
- [33] Ericson, F., Greek, S., Soederkvist, J., and Schweitz, J. A., "High Sensitivity Surface Micromachined Structures for Internal Stress and Stress Gradient Evaluation," *Journal of Micromechanical Microengineering*, Vol. 7, 1997, p. 30.
- [34] de Boer, M. P., Smith, N. F., Masters, N. D., Sinclair, M. B., and Pryputniewicz, E. J., "Integrated Platform for Testing MEMS Mechanical Properties at the Wafer Scale by the IMaP Methodology," *Mechanical Properties of Structural Thin Films, STP 1413*, S. B. Brown and C. L. Muhlstein, Eds., American Society for Testing and Materials, West Conshohocken, PA, 2001.
- [35] Gere, J. M., and Timoshenko, S. P., *Mechanics of Materials, 3rd ed.*, Boston: PWS, 1990.
- [36] Chai, H., Babcock, C. D., and Knauss, W. G., "One Dimensional Modeling of Failure in Laminated Plates By Delamination Buckling," *International Journal of Solid Structures*, Vol. 17, No. 11, 1981, p. 1069.

### Appendix A – Pointers

The relationship of residual stress to displacement for pointers was derived by van Drieënhuizen et al. [7]. In the analysis, the device is treated as a rigid body mechanism. Ideal rotational points, or hinges, are assumed, allowing the deflection to be based purely on geometry. A correction factor is then applied to account for hinge compliance. The layout of pointers is shown in Fig. A1. After release from the substrate, the angles in Fig. A2 are calculated as follows:

$$\tan(\phi_1) = \frac{O}{-\varepsilon_R L_A + L_B + W}, \quad (\text{A1})$$

$$\cos(\phi_2) = \frac{[(1 + \varepsilon_R)^2 + 1] + (1 + \varepsilon_R)^2 W^2 - (1 + \varepsilon_R)^2 L_B^2 + (-\varepsilon_R L_B + L_B + W)^2}{2\{[(1 + \varepsilon_R)^2 O^2 + (1 + \varepsilon_R)^2 W^2][O^2 + (-\varepsilon_R L_A + L_B + W)^2]\}^{1/2}}, \quad (\text{A2})$$

$$\tan(\phi_3) = \frac{W}{O}, \quad (\text{A3})$$

$$\text{and } \alpha = \phi_1 + \phi_2 + \phi_3 - 90^\circ, \quad (\text{A4})$$

where  $L_A$  and  $L_B$  are the lengths of the support beams (for this study they are equal),  $W$  is the pointer width,  $O$  is the distance between the turning points and  $\epsilon_R$  is the residual strain. The primes ( $L_A'$ ,  $L_B'$  etc.) in Fig. A2 indicate strain-relaxed lengths of members.

If  $W \ll (L_A$  and  $L_B)$  and if  $\cos(\theta) \approx 1$  (true if  $L_B \gg O$ ), then the strain may be approximated by

$$\epsilon_R = \frac{O \tan(\alpha)}{L_A + L_B}, \quad (\text{A5})$$

$$\text{and } \tan(\alpha) = \frac{y}{L_C + O/2}, \quad (\text{A6})$$

where  $y$  is the displacement of the indicator.

This allows a linear relationship between the displacement of the pointer,  $y$ , and the residual strain. Based on finite element modeling, a correction factor,  $C_F$ , is also included.

$$\epsilon_R = \frac{Oy}{(L_A + L_B)(L_C + O/2) C_F}. \quad (\text{A7})$$

## Appendix B – Bent-beams

Bent-beams use geometry to amplify the small displacements due to residual stress. By using two opposing bent-beam structures the measured deflection is double the deflection of an individual bent-beam, increasing sensitivity. This analysis will use Castigliano's method [20], which assumes that all deflections remain linearly elastic, in-plane, and that material properties are homogeneous. These assumptions are valid because the deflections are small and polysilicon is elastically homogeneous at the length scale of the test structures. The analysis considers a single bent-beam ("One-Half" model) subject to an effective axial force,  $F$ , as shown in the top diagram of Fig. B1. The effective force,  $F$ , facilitates correlation between the residual strain and deflection of the indicator. At this stage the deflection due to the strain in the indicator is neglected (second diagram, Fig. B1), but will be added later.

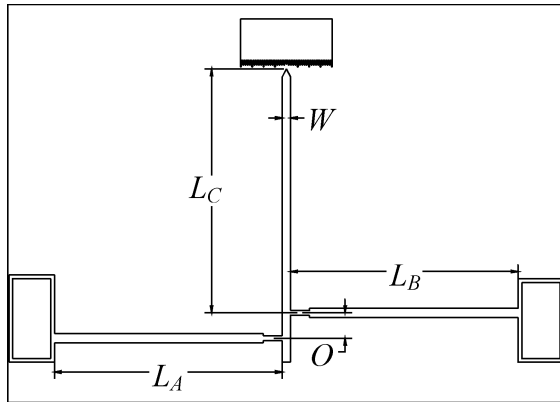


FIG. A1—Pointer Structure

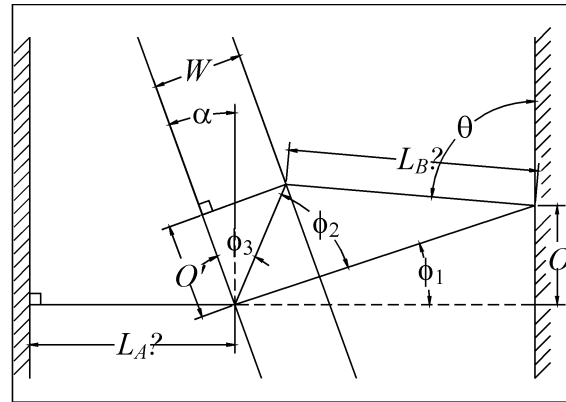


FIG. A2—Geometry of Pointers

By symmetry the bent-beam may be reduced to a fixed-guided member as shown in the third diagram (or “One-Quarter” model) of Fig. B1. The loading condition of a fixed-guided beam may be represented by point loads and an applied moment as shown in the final diagram of Fig. B1. The force  $Q$  is a virtual load used in Castigliano’s method to evaluate the deflection of the beam in the direction of  $Q$  (which is the direction of the measured indicator displacement).

The top diagram of Fig. B2 shows how the model is further simplified (using the symmetry of a fixed-guided segment) to a simple cantilever beam (length =  $L/2$ ) with point loads. The deflection of the complete bent-beam will be double that of this “One-Eighth” model. The middle diagram of Fig. B2 shows how the indicator may now be modeled by treating it as a segment having the same cross section as the support beams and susceptible only to axial deflections. This allows the axial strain of the modeled indicator to be equal to that of the support beams. Finally the coordinate axes are rotated to simplify the form of the derivation. The bottom diagram of Fig. B2 shows the model that will be used for the analysis.

$L_b$  is the actual length of the support beam (as used in the "One-Eighth" model), equal to  $L_{BB}/(2\cos\phi)$ , where  $L_{BB}$  and  $\phi = \arctan((D_0-D)/2L_{BB})$  are as indicated in Fig. 1. The functions for the moment and axial load along the beam and the axial load in the indicator are:

$$M_b(x) = (F \sin \phi + Q \cos \phi)x , \tag{B1}$$

$$P_b(x) = (F \cos \phi - Q \sin \phi) , \tag{B2}$$

$$\text{and } P_{Ind} = F . \tag{B3}$$

where  $M_b(x)$  is the bending moment along the support beam.  $P_b(x)$  is the transverse bending force and  $P_{Ind}$  is the axial force on the indicator.

The total elastic energy,  $U$ , of the deflected system of the one-eighth model is determined by the following integral (see Ref 20):

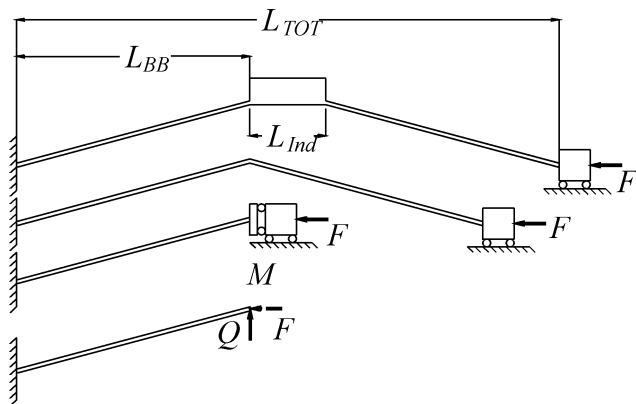


FIG. B1—Bent beams One-Half and One-Quarter Models.

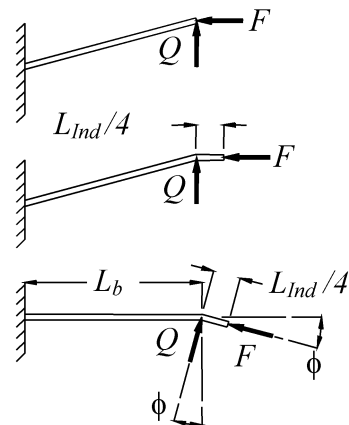


FIG. B2—Simplified model for Castigliano’s theorem evaluation.

$$U = \int_0^{L_b} \frac{M_b^2}{2EI_{yy}} dx + \int_0^{L_b} \frac{P_b^2}{2EA} dx + \int_0^{(L_{Ind}/4)} \frac{P_{Ind}^2}{2EA} dx. \quad (B4)$$

where  $E$  is the modulus of elasticity,  $I_{yy}$  and  $A$  are the in-plane moment of inertia and area of the effective beam cross section (in the configuration used in this study the support beams are composed of two beams each, thus  $I_{yy} = 2b^3t/12$  and  $A = 2bt$ ). Transverse shear effects are negligible because support beams are long and slender.

By Castigliano's theorem, the deflections (in the directions of  $Q$  and  $F$ ) are calculated by taking the derivative of the energy integral with respect to the forces  $Q$  and  $F$ :

$$\delta_Q = \frac{\partial U}{\partial Q} = \frac{(F \sin \phi + Q \cos \phi)L_b^3 \cos \phi}{3EI_{yy}} - \frac{(F \cos \phi - Q \sin \phi)L_b \sin \phi}{EA}. \quad (B5)$$

$$\delta_F = \frac{\partial U}{\partial F} = \frac{(F \sin \phi + Q \cos \phi)L_b^3 \sin \phi}{3EI_{yy}} + \frac{(F \cos \phi - Q \sin \phi)L_b \cos \phi}{EA} + \frac{FL_{Ind}}{4EA}. \quad (B6)$$

The virtual force,  $Q$ , is now set to zero and Eq B5 is solved for  $F$  in terms of  $\delta_Q$ , the deflection in the direction of  $Q$  (the displacement of the indicator)

$$F = \frac{3EI_{yy}A\delta_Q}{[AL_b^3 - 3IL_b] \sin \phi \cos \phi}. \quad (B7)$$

This is substituted into Eq B6, yielding a function for  $\delta_F$ , the deflection in the direction of  $F$  (the strain induced deflection), in terms of  $\delta_Q$ , such that

$$\delta_F = \left[ \frac{\delta_Q}{AL_b^3 - 3I_{yy}L_b} \right] \left[ AL_b^3 \tan \phi + 3IL_b \cot \phi + \frac{3I_{yy}L_{Ind}}{4 \sin \phi \cos \phi} \right]. \quad (B8)$$

The strain of such a deflection is the total deflection (for the "Half model") divided by the total length of the device, as in the following equation,

$$\epsilon_R = \frac{4\delta_F}{L_{TOT}} = \frac{4\delta_F}{2L_{BB} + L_{Ind}}. \quad (B9)$$

Substituting Eq B8 into Eq B9 and setting  $L_b = L_{BB}/2\cos\phi$  and  $\delta_Q = \delta/4$ , we obtain

$$\epsilon_{res} = \delta \frac{\left[ \frac{AL_{BB}^3 \sin \phi}{\cos^4 \phi} + \frac{12I_{yy}L_{BB}}{\sin \phi} + \frac{6I_{yy}L_{Ind}}{\sin \phi \cos \phi} \right]}{\left[ (2L_{BB} + L_{Ind}) \left( \frac{AL_{BB}^3}{\cos^3 \phi} - \frac{12I_{yy}L_{BB}}{\cos \phi} \right) \right]}. \quad (B10)$$

Eq B10 for the cases  $L_{Ind} = 0$  and  $L_{Ind} = 98 \mu\text{m}$  is compared to Gianchandani's rigorous derivation in Fig. 2 in the main body (with other parameters as indicated). For residual stress near zero, the results between the rigorous and linearized derivation with  $L_{Ind} = 0$  agree. The correction including  $L_{Ind} = 98 \mu\text{m}$  leads to a 15% increase in the slope,

meaning that for a given reading of  $\delta$ , the value of residual stress will be 15% lower. A 2-D finite element model that included non-linear deflections was developed in ANSYS to confirm the linear bent-beam model presented here. The results of the linear model were found to be within 2% of those obtained from the FEA model for strains within the range encountered in this study.

It should be noted that Eq B10 is more quickly applied than the rigorous derivation. The derivations in refs. [8,9] include strain stiffening, which is not accounted for in the present analysis. This omission simplifies the derivation of Eq B10, but as such Eq B10 does not account for nonlinearities at higher stress levels. On the other hand, Gianchandani's derivation does not account for the effect of the indicator length on the apparent stress as his structures were designed with indicator of negligible length. The sensors used here are taken from the design of Zavracky [9] who used indicators of substantial length, and therefore their length should not be neglected.

In tension, the effect of axial elongation and stress stiffening on  $\delta$  become greater than 10% at a strain value of +235  $\mu\epsilon$  (for the parameters used in Fig. 2). In compression, the axial elongation component is negligible compared to the bending contribution, and therefore the rigorous and linearized derivation with  $L_{Ind} = 0 \mu\text{m}$  agree within 10% to -312  $\mu\epsilon$ . Beyond this value, the nonlinear analysis becomes important because of loss of sensitivity inherent in the bending contribution. From this comparison we deduce that the linear model with  $L_{Ind} = 98 \mu\text{m}$  is valid over the range from -312 to 235  $\mu\epsilon$  (for  $L_{BB} = 300$  and  $(D_o - D)/2 = 10$ ). It should be noted that neither of these analyses takes buckling into account. If  $I_{zz} > I_{yy}$ , (as for Poly1 and Poly1/2 here), out-of-plane buckling is not expected. However, if  $I_{zz} < I_{yy}$ , buckling is complicated because out-of-plane buckling is favored by lower  $I_{zz}$ , but in-plane buckling is favored by  $\phi$ . A simple way to evaluate out-of-plane buckling is by interferometry, as discussed in the main text.

In short, for the values of stress encountered here (from -50 to -130  $\mu\epsilon$ ), Eq B10 with  $L_{Ind} = 98 \mu\text{m}$  gives the best values of residual stress. However, buckling is not accounted for, and may occur in Poly2 at values beyond  $-(\pi t/L)^2/3 = -45 \mu\epsilon$ , the critical strain for out-of-plane buckling for this layer. Higher sensitivity is possible at low  $\phi$  at the expense of a greater likelihood of buckling.

### Appendix C – Microrings

The analysis of microrings, as presented by Guckel et al. [10], uses Castigliano's method to calculate the residual strain from the radius of the critical ring. The following is a brief overview of that derivation. In the first step, the conversion efficiency,  $g(R)$ , is found from the following formulae:

$$g(R) = -(2b_r f_2) / (2b_r f_1 + b_b f_1^2 - b_b f_2^2), \quad (\text{C1})$$

$$f_1 = (\pi/4 - 2/\pi)(R/e) - 2e/\pi R + 4/\pi - \pi/4 + \pi k_f(1+\nu)/2, \quad (\text{C2})$$

$$f_2 = (1/2 - 2/\pi)(R/e) - 2e/\pi R - 1/2 + 4/\pi - k_f(1+\nu). \quad (\text{C3})$$

Definitions of the geometrical parameters  $b_r$  and  $b_b$  can be found in Fig. C1. The

constant  $k_f$  is a form factor for transverse shear ( $k_f = 1.2$  for rectangular cross sections, see Appendix A.2. of Ref 10 for more explanation),  $\nu$  is Poisson's Ratio ( $\approx 0.23$  for polysilicon),  $R$  is the effective ring radius, and  $e$  is the eccentricity,

$$e = R - b_r / \ln(R_o/R_i). \quad (C4)$$

In the second step, the effect of boundary compliance due to ring torsion on the critical buckling strain  $\varepsilon_{cr}$  is calculated. The boundary stiffness (as defined by applied torque divided by rotation at the crossbeam to ring connection) for out-of-plane buckling (i.e., for crossbeams with  $b_b > t$  where  $t$  is the film thickness) is

$$\alpha_o = \frac{4c_r E b_r t^3}{\pi R (6c_r + 1 + \nu) [1 - 4(1 + \nu - 6c_r)^2 / \pi^2 (1 + \nu + 6c_r)^2]}. \quad (C5)$$

where  $c_r$  is the torsional coefficient for the rectangular cross sections of the ring (the “o” subscript on  $\alpha$  refers to out-of-plane). The torsional coefficient  $c_r$  is approximated to within 0.5% by

$$c_r = \frac{1}{3} - \frac{64}{\pi^5} \frac{t}{b_r} \tanh\left(\frac{\pi b_r}{2t}\right). \quad (C6)$$

For in-plane buckling ( $b_b < t$ ) the boundary stiffness is

$$\alpha_i = \frac{\pi E t b_r^3}{3R(\pi^2 - 8)} \quad (C7)$$

(the “i” subscript on  $\alpha$  now refers to in-plane).

Knowing  $\alpha$ , the beam buckling criterion is found by solving the following transcendental equation for  $kR$

$$kEI_b / \alpha + \tan(kR) = 0, \quad (C8)$$

where  $k^2 = P_{cr} / EI_b$ ,  $I_b = b_b t^3 / 12$  for out-of-plane buckling or  $t b_b^3 / 12$  for in-plane buckling, and  $P_{cr} = \varepsilon_{cr} E b_b t$ . In the case of out-of-plane buckling, for example, if  $b_r = 2b_b$ ,  $c_r = 1/3$  and  $\nu = 0.23$ , from Eqs C5 and C8,

$$\tan(kR) = -0.3098kR, \quad (C9)$$

resulting in  $kR = -2.485$  and  $\varepsilon_{cr} = t^2 (kR_{cr})^2 / 12R_{cr}^2 = 0.515 (t / R_{cr})^2$ , where  $R_{cr}$  is the radius of the first buckled ring. The tensile strain may now be calculated by dividing the critical buckling strain by the conversion efficiency resulting in

$$\varepsilon_R = \frac{\varepsilon_{cr}}{g(R_{cr})} = \frac{(kR)^2 (t/R_{cr})^2}{12g(R_{cr})} = 0.515 \frac{(t/R_{cr})^2}{g(R_{cr})}. \quad (C10)$$

### Appendix D – Fixed-fixed Beams

The governing equation for an elastically buckled beam supported by fixed clamps, assuming small slopes, is [35]

$$z''(x) + k^2 z(x) = M_o / (EI), \quad (D1)$$

where  $k^2 = P/EI$ ,  $I = b_{FF}t^3/12$ ,  $P$  is the axial load in the beam and  $M_o$  is the end moment supported by the clamps. The clamped boundary conditions are

$$z(-L_{FF}/2) = z'(-L_{FF}/2) = z(L_{FF}/2) = z'(L_{FF}/2) = 0. \quad (D2)$$

The general solution satisfying Eqs. (D1) and (D2) is

$$z(x) = \frac{A}{2} \left( 1 + \cos \frac{2\pi n x}{L_{FF}} \right), \quad n = 1, 3, 5, \dots \quad -L_{FF}/2 \leq x \leq L_{FF}/2. \quad (D3)$$

where  $A$  is the amplitude of the buckled beam. The only solution of practical interest, representing the smallest critical load,  $P_{cr}$ , is for  $n = 1$ . Then,  $k = 2\pi/L_{FF}$  and  $P_{cr} = EI(2\pi/L_{FF})^2$ , giving a critical buckling strain  $\varepsilon_{cr}$  of

$$\varepsilon_{cr} = \frac{P_{cr}}{Eb_{FF}t} = \frac{\pi^2 t^2}{3L_{FF}^2}. \quad (D4)$$

The amplitude  $A$  can be related to the residual strain in the unbuckled beam in light of the following two considerations [36]. First, the length of the buckled beam can be determined from the arc length formula by using the small angle approximation (as

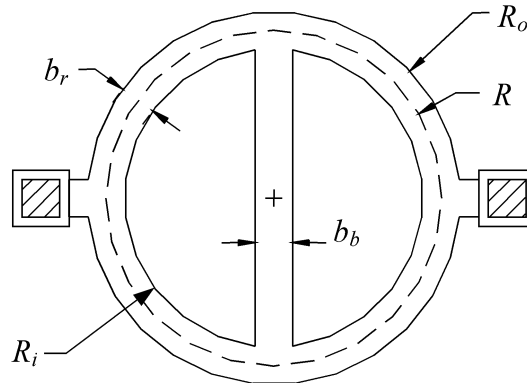


FIG. C1—Microring diagram.

justified by the assumption of small slopes),

$$l_{beam} = \int_{-L_{FF}/2}^{L_{FF}/2} \left[ 1 + \left( \frac{dz}{dx} \right)^2 \right]^{1/2} dx \approx L_{FF} \left[ 1 + \left( \frac{A\pi}{2L_{FF}} \right)^2 \right]. \quad (D5)$$

Second, for the assumption of small slopes, the stress in the buckled beam is equal to the buckling stress. Then, the residual strain released by buckling (i.e., the strain that contributes to a change in length of the beam) is

$$\delta\varepsilon = \varepsilon_R - \varepsilon_{cr}. \quad (D6)$$

where  $\varepsilon_R$  is the residual strain in the material. Therefore, the length of the buckled beam may also be expressed as

$$l_{beam} = L_{FF} (1 + \delta\varepsilon) = L_{FF} (1 + \varepsilon_R - \varepsilon_{cr}). \quad (D7)$$

From Eqs D5 and D7, and using Eq D4, we obtain

$$\varepsilon_R = \frac{A^2\pi^2}{4L_{FF}^2} + \frac{\pi^2 t^2}{3L_{FF}^2} = \frac{\pi^2}{12L_{FF}^2} (3A^2 + 4t^2). \quad (D8)$$

Both  $A$  and  $t$  can be accurately measured, and  $L_{FF}$  is well-known from the layout dimensions. Considering that the elastic supports built by surface micromachining methods are typically relatively stiff, Eq D8 gives excellent results for the measurement of  $\varepsilon_R$  using beams of lengths somewhat larger than the ideal critical Euler buckling length  $L_{cr}$ , i.e.,

$$L_{FF} \gg 1.1 L_{cr} = 1.1 \left( \frac{\pi t}{\sqrt{3\varepsilon_{cr}}} \right), \quad (D9)$$

where we have rearranged Eq D4 to find  $L_{cr}$ . In Eq D9, we have used Fig. 4 in the main body to assign the 10% length correction compared to the ideally clamped boundary case. Note that the greater the value of  $L_{FF}$  with respect to  $L_{cr}$ , the smaller is  $M_o$ , and the lesser the effect of any boundary compliance on the deflection curve. Therefore, because the small slopes assumption remains valid, as  $L_{FF}$  grows large compared to  $L_{cr}$ , Eq D8 correspondingly improves in accuracy.